Linking simple molecules to grain evolution across planet-forming disks

Salinas Poblete, V.N.

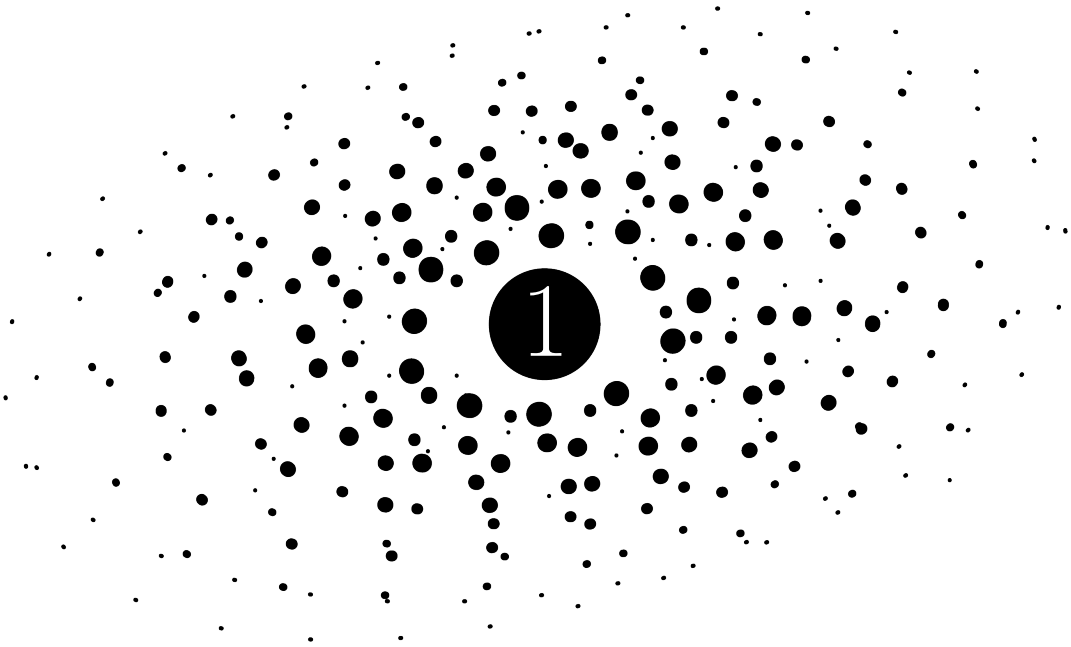

1 Introduction

Our very existence as sentient beings has prompted us to question our place in the Universe. Ancient transcendental questions have found their way into astronomy in the following forms: What are the conditions for life? How did our Solar System form? How did the Earth form? How do other planets form? What sets the chemical composition and the ingredients for life throughout the star and planet formation process? The very first attempt to understand the formation of our Solar System was made by the French mathematician and philosopher René Descartes in his book 'Traité du monde et de la lumière'. His publication was delayed several years, feared by the Roman Inquisition because of its heliocentric view of the Universe, but was finally made available post-mortem in 1664. His theory comprised of colliding corpuscular particles in space, constantly swirling around in a continuous fashion with no vacuum inbetween. The continuous nature of his colliding particles provided the necessary force for the movement of planets around the Sun. Although incorrect, his work paved the way for the generally accepted Nebular Hypothesis, formulated first by Emanuel Swedenborg and expanded by Immanuel Kant in 1755 and (independently) by Pierre-Simon Laplace in 1796. This hypothesis consisted of a gaseous cloud of matter slowly collapsing and rotating, eventually becoming flat due to gravity, culminating in the formation of the Sun and planets.

Two more centuries had to pass until the first empirical evidence supporting this theory was discovered. Low-mass T Tauri stars (Herbig 1977) and other young objects (Cohen & Kuhi 1979) were first observed in the infrared (IR) and optical regimes. The observed IR excess could only come from material at much lower temperatures than the star. A major breakthrough came a decade later when the InfraRed Astronmical Satellite (IRAS) detected the first circumstellar disk around Vega. Although this is a rather old disk, many other young objects were found to harbor circumstellar disks through subsequent surveys by IRAS, ISO, the *Hubble Space Telescope* and the *Spitzer Space Telescope* in many star formation regions.

The next decade brought the discovery of the first planet orbiting a star other than the Sun, 51 Pegasi (Mayor & Queloz 1995). In the last two decades more than 3000 exoplanets, and about 2000 more candidates, have been found. Now that we are certain of the existence of exoplanets, and that most of the young stellar objects (YSOs) contain circumstellar material, the scientific community has been trying to understand the processes involved in the formation of planets. The study of so-called protoplanetary disks aims to explain the missing link between star formation and planet formation and the composition of other planetary systems as well as our own Solar System's history. This thesis will focus on understanding the processes that shape the distributions of key molecular species, such as water and ammonia, and simple deuterated species, by contrasting them with the spatial structures produced by dust evolution, photo-processes and gas-phase chemistry.

1.1 Disk formation

1.1.1 Collapse phase

The first step toward understanding the formation of planets is understanding the formation of circumstellar disks. The star formation process starts with a gravitationally unstable molecular cloud that collapses first onto a hydro-static core due to gravity (Ebert 1955; Bonnor 1956; Jeans 1902). A rotationally supported disk quickly forms within 10^4 yrs (Yorke et al. 1993; Hueso & Guillot 2005) as more distant material, with higher angular momentum, falls in (Figure 1.1). At this stage, the newly formed disk is fully embedded in an envelope of gas and dust. The rotation of the envelope has been measured up to scales

of ~ 0.1 pc (Goodman et al. 1993), with typical rotation rates of 10^{-15}–10^{-12} Hz (Burkert & Bodenheimer 2000; Dib et al. 2010). Infall models were first used by Ulrich (1976) to describe the continuum and line-emission features of T Tauri disks. The viscous accretion disk theory (Lynden-Bell & Pringle 1974; Shakura et al. 1978) was later used to derived a formalism of the radial structure of disks in the context of star formation considering conservation of mass, momentum and energy (Cameron 1978; Cassen & Moosman 1981; Terebey et al. 1984)

Molecular clouds have typical specific angular momenta of ~ 10^{21-22} cm^2 s^{-1} (Goodman et al. 1993), which is 6-7 orders of magnitude higher than that of the Sun (Pinto et al. 2011). The removal of the angular momentum can be achieved through winds and jets or through viscous accretion. The disk viscosity is mainly dominated by the mixing of fluid elements. Several processes, such as magnetorotational instability (MRI), have been proposed as the dominating mechanisms driving the viscous transport through the disk (for a review, see Armitage 2011). The efficiency of the MRI depends on the degree of ionization because it requires the gas and the magnetic field to be well coupled. However, protoplanetary disks are only weakly ionized. Moreover, MRI is damped or suppressed by non-ideal magentohydrodynamical effects and a magnetized disk wind has been recently suggested as the primary mechanism driving disk accretion (Bai 2016, and references therein). It is important to notice that magnetic fields could also dissipate angular momentum at large scales, since the beginning of the collapsing phase, through twisted magnetic field lines (Königl & Salmeron 2011) but the efficiency of this process is not clear. The wide range of initial angular momenta and variations in the infall duration give birth to disks that are different in size and mass (Terebey et al. 1984).

1.1.2 Embedded phase

The embedded phase typically lasts ~0.5 Myr (Evans et al. 2009; Carney et al. 2016). Infall describes the trajectory of material from the envelope to the disk while the material of the disk is slowly accreted onto the protostar. The disk is heated through both the infall process and the accretion. The accretion rate of material being transported into the protostar is crucial to determine the dust temperature structure of the disk and the inner envelope at this stage. This process is probably episodic to avoid the luminosity problem (see Kenyon & Hartmann 1990; Evans et al. 2009; Dunham et al. 2014). This problem concerns the discrepancy between the observed low luminosity of embedded objects and the higher luminosity predicted by accretion at a constant rate. Episodic accretion models can transfer sufficient mass to the central star without requiring sustained accretion rates larger than observed. The material of the core's envelope is gradually dispersed through outflows and jets or accreted on the disk. Eventually, the outflows produce a cavity in the envelope that grows to leave a disk behind (see work by Velusamy & Langer 1998; Arce & Sargent 2004, 2006; Salter 2010; Harsono 2014).

1.1.3 Observational characterization

The protostellar stages leave distinctive observational features that can be used to classify them. The first method proposed by Lada (1987) classifies YSOs into three different classes (I-II-III see Table 1.1) by measuring the slope of the spectral energy distribution (SED) in the mid-IR. This classification was later expanded to include a class 0 as new instruments were able to detect weaker (sub)millimeter emission of more deeply embedded objects (André et al. 1993).

Table 1.1: Classification of young stellar objects, taken from Williams & Cieza (2011).

Class	Physical properties	Observational characteristics
0	$M_{\rm env} > M_{\rm star} > M_{\rm disk}$	No optical or near-IR emission
I	$M_{\rm star} > M_{\rm env} \sim M_{\rm disk}$	Generally optically obscured
II	$M_{\rm disk}/M_{\rm star} \sim 1\%$, $M_{\rm env} \sim 0$	Accreting disk; strong Hα and UV
III	$M_{\rm disk}/M_{\rm star} \ll 1\%$, $M_{\rm env} \sim 0$	Passive disk; no or very weak accretion

1.2 Physical properties of protoplanetary disks

After the end of Class I the disk is no longer embedded and the disk mass is only a small fraction of the stellar mass. The beginning of Class II marks the end of the star formation phase and the circumstellar disk can be considered truly planet forming and not protostellar. Protoplanetary disks have a rich and complex physical structure. This section describes the quantities that characterize planet-forming disks.

1.2.1 Mass

Traditionally, disk masses have been determined from the thermal emission of the dust, and multiplied by an assumed gas-to-dust mass ratio of 100. The (sub)millimeter emission arises from the thermal emission of the dust particles. As a rule of thumb, observations at a wavelength λ are only sensitive to the properties of dust grains of a maximum size $a_{\rm max} \sim 3\lambda$ (Draine 2006). The dust dominates the opacity (κ_ν) at (sub)millimeter wavelengths and we can express the dependency of its emission on the frequency as a power law $\kappa_\nu \propto \nu^\beta$. A commonly used prescription for the dust opacity is given by Beckwith et al. (1990) and Hildebrand (1983),

$$\kappa_\nu = 0.1 \left(\frac{\nu}{10\text{MHz}} \right)^\beta \text{cm}^2\text{g}^{-1}. \tag{1.1}$$

In the Rayleigh-Jeans limit, the spectral index α is related to the opacity index β by the following expression

$$\alpha = 2 + \beta. \tag{1.2}$$

The typical value for the opacity index of interstellar dust material is $\beta_{\rm ISM} \sim 1.7$. A power-law dust size distribution of the form $n(a) \propto a^{-3.5}$ (Mathis et al. 1977) that has experienced grain growth, up to a maximum particle size of $a_{\rm max} = 1$ mm, results in $\beta \lesssim 1$. We can then

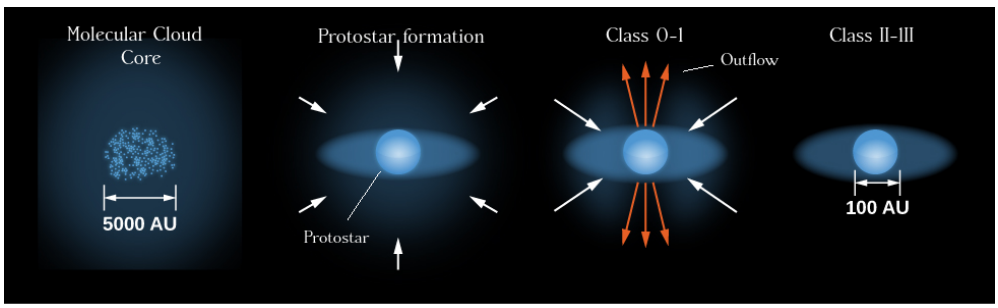

Figure 1.1: Cartoon showing the star and disk formation process. Adapted from LibreText Physics: Astronomy and Cosmology Textmaps:21.1 Star Formation (https://phys.libretexts.org/).

use Eq.1.2 for the spectral index as a diagnostic of grain growth at millimeter wavelengths. Continuum observations at multiple wavelengths are required for the extraction of the α parameter.

If we assume that most of the emission arises from optically thin material in the (sub)mm regime, a useful expression can be derived to calculate the disk mass by assuming a characteristic temperature T_c (Williams & Cieza 2011)

$$M(gas + dust) = \frac{F_\nu d^2}{\kappa_\nu B_\nu(T_c)}, \tag{1.3}$$

where d is the distance to the source, B_ν is the Planck function, F_ν the millimeter flux and κ_ν is the mass opacity that assumes a given gas-to-dust ratio. Detailed modelling of the mid-IR SED of disks towards the Ophiuchus region carried by Andrews & Williams (2005) showed that Eq. 1.3 is indeed a good approximation.

A number of caveats have to be taken into consideration when using Eq.1.3 to determine the disk mass. First, a large portion of the disk mass could be hidden in grains larger than a centimeter. The millimeter emission is not sensitive to this grain population. For the power-law grain size distribution given above, the total mass scales as $a_{max}^{1/2}$. Second the opacity index β depends on the size distribution of the dust particles (Ossenkopf & Henning 1994; Pollack et al. 1994; D'Alessio et al. 2001). As discussed above dust evolution processes, such as grain growth, can significantly change the opacity κ_ν at the (sub)millimeter regime. Finally, this method indirectly assumes a gas-to-dust ratio, canonically taken to be equal to the ISM value of 100; an assumption that might not hold for evolved disks. Disk masses derived from accretion rates and disk life-times are in the range of 0.01-0.2 $M_\odot$ (Hartmann et al. 1998) while the inferred disk masses in Taurus from continuum observations using a gas-to-dust ratio of 100 show a median value of 5×10^{-3} $M_\odot$ (Andrews & Williams 2005).

Observing more direct gas tracers, such as CO, can constrain the disk mass without the assumption of a gas-to-dust ratio. Disk masses derived from less abundant CO isotopologues, that are optically thin, toward a sample of T Tauri disks are on average below the Minimum Mass Solar Nebula (MMSN) of 10^{-2} $M_\odot$ (Williams & Best 2014) and their average gas-to-dust ratio of 16 is 6 times lower than in the ISM. The observations of other planetary systems suggest that disk masses larger than the ones derived by these methods are required to form many of the extrasolar planet systems (Greaves & Rice 2010; Mordasini et al. 2012). Although these results do not depend on an assumed gas-to-dust ratio they do depend on the assumed relative abundance of the CO and its isotopologues to H_2 (Miotello et al. 2016). A correct determination of the disk mass is essential to determine the potential of a protoplanetary disk to form planets. Recently HD, whose abundance is more directly correlated to that of H_2, has been used to constrain the mass of the disk around TW Hya (Bergin et al. 2013). Unfortunately the emission of HD lines is usually weak, cannot be observed from the ground and is only sensitive to warm gas.

Observations in the (sub)millimeter regime of disks around Class II YSOs show a positive correlation between disk mass and stellar mass (Natta et al. 2000; Andrews et al. 2009; Lee et al. 2011; Andrews et al. 2013; Williams et al. 2013; Ansdell et al. 2015, 2016, 2017). This behavior is expected since higher mass stars require more material to pass through the disk. For more massive stars this correlation breaks down. The Orion proplyd survey (Mann & Williams 2009) constrains this relation to $M_{disk}/M_{star} \lesssim 10^{-4}$ for stellar masses $> 2M_\odot$. No signature of (sub)millimeter emission has been detected around optically visible O stars. This could be due to very high photoevaporation rates or to a totally different star-formation mechanism (Zinnecker & Yorke 2007). Enviromental influences, such as dynamical disruption in binaries or by another passing star (Pfalzner et al. 2005a,b; Thies

et al. 2010) or photoevaporation by massive stars (Bally et al. 2000; Adams et al. 2004) can influence the size and mass of the disk.

1.2.2 Radial structure

The radial distribution of the mass of the disk can be described through its surface density $\Sigma(r)$, defined as

$$\Sigma(r) = \int_{-\infty}^{\infty} \rho(r,z)dz, \tag{1.4}$$

where ρ is the density of the disk in cylindrical coordinates. We can derive an analytical expression of $\Sigma(r)$ by looking at the radial component of the viscous accretion model of Shakura et al. (1978),

$$\frac{\partial \Sigma}{\partial t} + \frac{1}{r}\frac{\partial(\Sigma r v_r))}{\partial r} = 0, \tag{1.5}$$

$$v_r = -\frac{3}{\Sigma\sqrt{r}}\frac{\partial}{\partial r}\left(\Sigma\nu\sqrt{r}\right), \tag{1.6}$$

$$\nu = \alpha\frac{c_s^2}{\Omega_K} \tag{1.7}$$

where Eqs. 1.5, 1.6, 1.7 are obtained by integrating the continuity, radial momentum and tangential momentum equation over z respectively, v_r is the radial component of the velocity, Ω_K is the Keplerian angular velocity, α is an dimensionless parameter characterizing the turbulence of the disk and the speed of sound c_s is a function of the temperature of the disk. A constant $\alpha \sim 0.01$ reproduces the observed disk evolution and physical structure of protoplanetary disks (Hartmann et al. 1998; Hughes et al. 2011). If we take as ansatz that both the surface density and the temperature are power-laws of the form $\Sigma(r) \propto r^{-p}$ and $T(r) \propto r^{-q}$ respectively the solution for the steady-state of Eq. 1.5 is $\Sigma(r) \propto r^{q-3/2}$. The temperature power-law index q is equal to 3/4 considering only viscous heating, but flattens to $q = 1/2$ at larger radii where the temperature profile is dominated by stellar irradiation (see Sec. 1.2.4). This leads to a radial distribution of the mass of the disk with power-law indexes ranging from $p \sim 1 - 3/4$.

Resolved millimeter observations of disks allow to constrain the radial distribution of the dust material. The radial extent of the disk is difficult to constrain since it emits faintly due to low temperatures and column densities in the outer regions. In the optical regime the outer parts of the disk can be seen in absorption. The *Hubble Space Telescope* found that on average disk sizes toward the Orion region are $\sim$ 75 AU (Vicente & Alves 2005). Until recently most of the disks were modeled as pure power-laws but observations of CO and the millimeter continuum are difficult to reconcile with such a simple treatment. CO observations are consistently more extended than the continuum emission at millimeter wavelengths (Piétu et al. 2005; Isella et al. 2007; Panić et al. 2009; Isella et al. 2016) and a sharp cut-off of the surface density power-law is unable to explain both observations without relying on changing the gas-to-dust ratio or dust opacity at the edge of the continuum emission. A exponential taper at a characteristic radius R_c was needed to explain this behavior (McCaughrean & O'dell 1996; Hughes et al. 2008) of the form

$$\Sigma(r) = (2-\gamma)\frac{M_d}{2\pi R_c^2}\left(\frac{r}{R_c}\right)^{-\gamma}\exp\left[-\left(\frac{r}{R_c}\right)^{2-\gamma}\right]. \tag{1.8}$$

This solution of Eq. 1.5 is known as the self-simlar solution (Lynden-Bell & Pringle 1974), and is different from the single power-law solution because it considers the viscous coefficient ν to be a power-law with exponent γ.

1.2.3 Vertical structure

Disks are not flat. Observational evidence can be found in the Hubble images of scattered light from the central star forming characteristic silhouettes around disks in the Taurus and Orion regions (Burrows et al. 1996; Stapelfeldt et al. 1998; Padgett et al. 1999; Smith et al. 2005). The vertical distribution of dust and gas in protoplanetary disks follows from the balance between the gas pressure and the vertical component of the gravitational force. If we assume that the disk is geometrically thin, then the vertical structure is in quasi-static equilibrium compared to the timescales that govern the radial motion of the disk. The vertical temperature gradient is complex and depends on viscous energy dissipation and radiative transfer. But for simplicity, if we consider the disk to be isothermal in the vertical axis the hydro-static equilibrium equation is given by

$$\frac{kT}{\mu m_u}\frac{d\rho(z)}{dz} = -\rho(z)\Omega_K^2 z, \tag{1.9}$$

where k is the Boltzmann constant, μ is the mean molecular weight and m_u is the atomic mass unit. This has a Gaussian solution of the form

$$\rho(z) = \rho_0 \exp\left(-\frac{z^2}{2h(r)^2}\right) \quad \text{with} \quad h(r) = \sqrt{\frac{kT(r)r^3}{\mu m_p G M_{\rm star}}}, \tag{1.10}$$

where $h(r)$ is the scale height of the disk at a radius r, which depends on the competition between disk thermal pressure and the vertical component of stellar gravity. The disk thermal pressure depends on the amount of stellar radiation absorbed at the disk surface and it is discussed in the following section. The temperature dependence can be solved analytically by considering a hot surface layer that captures and reprocesses the starlight thereby heating the gas and resulting in a flared interior (Kenyon & Hartmann 1987; Natta 1993; Calvet et al. 1994; Chiang & Goldreich 1997). The scale height can then be parametrized as a power law of the form $h(r) \propto r^{\psi}$ with $\psi \sim 1.3 - 1.5$.

Flared disks reproduce the far-IR excess better than spatially flat disks (Kenyon & Hartmann 1987). All observed disks to date exhibit some degree of flaring, therefore they intercept and reprocess more stellar radiation than flattened disks. Most T Tauri stars exhibit less mid-IR emission than what is expected from a disk in hydrostatic equilibrium. This can be interpreted as a consequence of a reduced flaring angle due to settling of dust particles at very short timescales (see Sec.1.4.3). Observational evidence of settling in protoplanetary disks can be found by measuring the slope at mid-IR wavelengths (Chiang et al. 2001). The median mid-IR slopes of classical T Tauri stars imply that in these disks more than 90% of their μm-sized grains have settled into the midplane (D'Alessio et al. 2006).

1.2.4 Temperature structure

The temperature structure of disks is dominated by the mechanical heating produced by the viscous nature of the disk only in the innermost dense regions, reaching temperatures as high as 1000 K. The formalism derived by Shakura et al. (1978) considering only viscous heating and dissipation mechanisms such as thermal radiation and convection gives an

effective temperature for the disk as a function of radius of the form

$$T_{eff} \propto \dot{M}^{1/4} r^{-3/4}, \tag{1.11}$$

where $\dot{M}$ is the accretion rate of the star. If we consider a simple model for disk irradiation from the central star then the expression is modified to (Chiang & Goldreich 1997)

$$T_{eff} \propto \dot{M}^{1/4} r^{-3/4} + L_{\rm star}^{1/4} r^{-1/2}, \tag{1.12}$$

where $L_{\rm star}$ is the luminosity of the star. At the outer disk, for large r, the first term corresponding to the mechanical heating drops faster than the irradiation term. This effective temperature does not take into account the vertical structure of the temperature. The processing of stellar and external radiation by the dust material determines the vertical and radial temperature profile at large radii and in the upper layers of the inner disk (Dullemond et al. 2007; Hirose & Turner 2011). A two-layer approximation of this problem, which solves the vertical temperature gradient analytically, can be found in Appendix A of Chiang et al. (2001). Nowadays, many 2D and axisymmetric 3D models (pioneered by D'Alessio et al. 1998, in 1+1-D) solve the complete disk structure problem with diffusive radiative transfer, including stellar irradiation and viscous dissipation.

The computation of the temperature structure requires knowledge of the opacity, dominated by the dust for the iterative radiative process and many models calculate the temperature structure $T(r)$ self-consistently for a given dust density distribution (see Sec. 1.6.2). It is generally assumed that gas is well coupled with the dust thus $T_{\rm gas} = T_{\rm dust}$. This assumption is not valid within the super-heated surface layer of the disk but is true for most of the optically thick matter at the UV and IR regimes inside the midplane region of the disk where the gas density is sufficiently high. The gas temperature above the surface layer of the disk is determined by various heating and cooling processes. These processes depend on the chemical composition of main atomic and molecular species that in turn depend on the gas temperature. Some molecular species, such as H_2, CO or C_2H, probe the region where the gas is decoupled from the dust, but other species emit from deeper and colder regions where the aforementioned assumption is still valid.

1.2.5 Ultraviolet and X-Ray radiation

Protoplanetary disks are exposed to intense ultraviolet (UV) and X-ray radiation. For T Tauri disks, at 100 AU, the UV radiation from the accretion onto the star is a factor of 100-1000 stronger than in the ISM (Bergin et al. 2003). For the much hotter Herbig Ae disks ($M_{\rm star} > 2M_{\odot}$), the UV radiation has a photospheric origin and is factor of 10^5 stronger than the ISM (Semenov et al. 2005; Jonkheid et al. 2006). The median value for the X-ray luminosity of T Tauri stars is $\log(L_X/L_{\rm bol}) \approx 3.5$ or $L_X \approx 3 \times 10^{29}$ erg s^{-1}(Preibisch et al. 2005; Getman et al. 2009) which is generated by the magnetic activity produced due to the convective nature of the stellar interior. The more massive Herbig Ae stars are usually non-convective resulting in X-ray luminosities more than 10 times lower than those found in T Tauri stars (Güdel & Nazé 2009). Unlike UV radiation, X-rays can penetrate deeper in the disk and, together with cosmic rays, ionize He which is fundamental to drive chemistry. In the midplane, secondary UV radiation emitted by molecular hydrogen after ionization by X-rays or cosmic rays is the only UV source. The photo-processes triggered by UV and X-ray radiation, such as ionization and the release of radicals and free electrons, fuel the chemistry deep within the disk (see Sec.1.5).

1.3 Disk evolution

1.3.1 What happens to the gas?

Class III YSOs are characterized by weak far-IR emission coming from small cold dust that is left after most of the gas has been accreted into the central star or dissipated by stellar winds (Matsuyama et al. 2009) and/or FUV and X-ray radiation coming from the central star or external sources (Gorti et al. 2009; Owen et al. 2010). The evolution of the gas content in protoplanetary disks is driven, in a first order approximation, by viscous accretion. There is no single physical mechanism dominating the transport of angular momentum throughout the disk, although a magnetized disk wind has been recently suggested as the primary mechanism driving disk accretion (see Sec.1.1.1 and Bai 2016; Turner et al. 2014).

Extensive modeling of viscous transport, and in particular the α parameter as a representation of the turbulence that gives origin to viscosity, has been done in 3D including self-gravity and MRI as well as convection and planet-disk interaction (see references in Armitage 2011). Although this model correctly predicts observable accretion indicators, such as the Hα line, it fails at predicting the sudden and very quick disk dissipation that occurs after the typical disk lifetime of a few Myr (Fedele et al. 2010). Right after the accretion onto the central star stops, it is estimated that it only takes $\lesssim 0.5$ Myr to dissipate all the material from the primordial disk (Calvet et al. 2002; Cieza et al. 2007). The photoevaporation by UV and X-ray radiation from the central star overtakes viscous accretion in the outer regions of the disk, opening a gap and cutting off accretion, while the inner disk is rapidly accreted onto the star (Clarke 2007; Clarke et al. 2001). Immediately after, the outer disk is exposed to energetic UV photons and X-ray radiation and the disk is quickly photoevaporated form the inside out. A schematic of this process is shown in Fig. 1.2.

1.3.2 What happens to the dust?

In parallel, the dust also evolves to eventually form planets. More than 13 orders of magnitude separate the size of the interstellar dust with planets. The core accretion scenario (Safronov 1972; Lissauer 1993; Pollack et al. 1996; Haghighipour 2013) describe this process in three steps.

First, small grains coagulate to form cm-sized particles (Dullemond & Dominik 2005, 2008). Evidence for the formation of μm-sized particles is abundant, even at early stages, from amorphous silicate features in the IR (Kessler-Silacci et al. 2007; McClure et al. 2010). The evidence for millimeter and centimeter sized particles comes from the impact of opacity on the shape of the SED at millimeter wavelengths (Andrews & Williams 2005). As the population of centimeter sized particles grows, the dust opacity decreases and the slope of the SED becomes shallower at millimeter wavelengths (Natta et al. 2004; Draine 2006).

Second, the grains continue to grow to form km-sized bodies. This step is less understood than the previous one as it involves dynamical processes that arise due to the decoupling of gas and dust (Dubrulle et al. 1995; Birnstiel et al. 2011), namely settling and radial drift that are discussed in detail in the next section. Decoupled grains start experiencing a radial inward drift that is much faster than the coagulation time scales, thus preventing them from growing larger than a few meters. As dust particles begin to grow and the impact velocities increase, the outcome of their collisions results in bouncing. In the bouncing regime dust particles do not stick together but are compacted due to the collision. In addition, fragmentation of large dust grains, close to the inner regions of the disk, becomes efficient as the relative velocities between grains are enhanced by these dynamical processes (Weidenschilling 1984; Birnstiel et al. 2012). The combination of fragmentation,

bouncing and radial drift for meter-sized bodies is commonly called the meter-sized barrier.

A radial pressure maximum in the gaseous content of the disk, caused by density variations, is capable of stopping the radial migration of dust (e.g. Lyra et al. 2009; Brauer et al. 2008). Azimuthal vortices can arise once the dust has stopped migrating which are an effective way to trap the dust particles and allow them to grow (Pinilla et al. 2015). These vortices have been observed toward a couple of disks at millimeter wavelengths (e.g. van der Marel et al. 2013).

For a given distribution of dust sizes and velocities, some particles will collide with velocities that are below the critical velocities of the bouncing and fragmentation regimes. These 'lucky' particles can overcome the bouncing barrier and grow further (Garaud et al. 2013; Windmark et al. 2012). Collections of pebbles resulting from streaming instabilities in the disk can collapse to quickly form bodies as large as the asteroid Ceres in one step (Johansen et al. 2007). This process is a consequence of the so-called streaming instability and is an effective mechanism to concentrate dust particles at super-critical densities overcoming the fragmentation barrier.

Finally, once planetesimals of a few kilometers in size have formed, they grow further by sweeping up and gravitationally attracting smaller particles. At early stages of planetary accretion, the gravitational attraction of large planetesimals leads to runaway accretion while small planetesimals remain unchanged (Greenberg et al. 1978; Barnes et al. 2009). The resulting largest bodies, known as planetary embryos or protoplanets, start to dominate the viscous stirring produced by the gravitational scattering effect (Ida & Makino 1993). The formation of these large planetesimals at time scales shorter than the lifetime of the disk

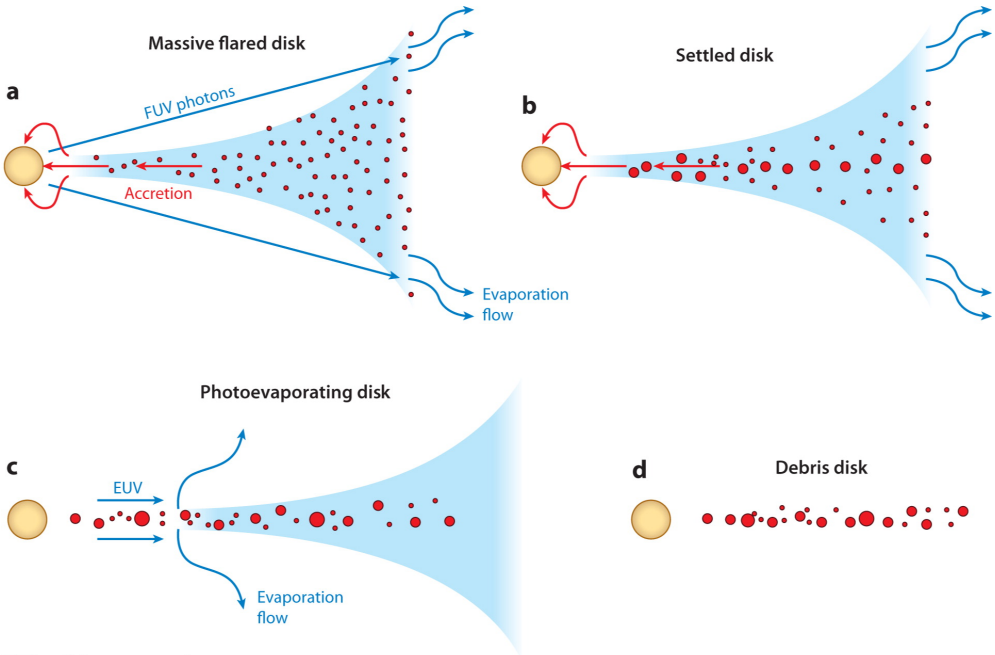

Williams JP, Cieza LA. 2011.
Annu. Rev. Astron. Astrophys. 49:67–117

Figure 1.2: Cartoon showing the evolutionary path of a disk around a low-mass star, taken from Williams & Cieza (2011)

is challenging, but mechanisms like pebble accretion can aid to overcome this problem (Ormel & Klahr 2010; Lambrechts & Johansen 2014). In the presence of gas, massive cores of several Earth masses attract a gaseous envelope to form Jupiter like planets (Lissauer et al. 2012; Lissauer 1993).

1.4 Dust in disks

Although dust particles contain only 1% of the initial mass of protoplanetary disks, they are the precursors of planets and are fundamental in the formation of complex molecules through grain-surface chemical reactions. Moreover, they dominate the opacity of the disk. In Sec. 1.3.2 we briefly discussed dust coagulation processes that allow (sub)micron dust particles to grow to millimeter/centimeter sized particles and their impact on dust opacity. The dynamical processes that shape the dust spatial distribution are different from the ones that affect the gas. This thesis focuses in understanding the link of the spatial distribution of dust grains of different sizes and the formation mechanism and spatial distribution of key volatiles in the gas. This section will focus on the physical processes that affect dust grains in disks and their composition.

1.4.1 Composition

Dust, in the diffuse ISM, is mainly composed of silicates with an admixutre of graphite grains and polycyclic aromatic hydrocarbons (PAHs) (Draine 2003). These are easily identified through spectral features at 10 and 18 μm (silicates, Henning et al. 2010) and through a series of features in the mid-IR (PAHs, Tielens 2008).

Observations of the disks around T Tauri and Herbig Ae/Be stars typically show spectral features corresponding to a mixture of amorphous silicates with olivine and pyroxene stoichiometry (being 1%-30% of the content), crystalline forsterite and enstatite, and in some cases silica (see references in Henning & Semenov 2013). In the warm inner regions of protoplanetary disks up to a few AU, the dust has been processed via thermal annealing or shock heating resulting in a higher crystallinity fraction (Harker & Desch 2002; van Boekel et al. 2005; Olofsson et al. 2009, 2010; Oliveira et al. 2011). Features of molecular ices, such as H_2O and CO_2, have been detected in absorption toward edge-on disks and in emission toward face-on disks, including the 63 μm feature of crystalline water (Malfait et al. 1999; Thi et al. 2002; Pontoppidan et al. 2005; Terada et al. 2007; Terada & Tokunaga 2017; Aikawa et al. 2012; McClure et al. 2012; Riviere-Marichalar et al. 2016). The freeze-out and desorption processes of the ice reservoir in protoplanetary disks are further discussed in Sec.1.5.1.

1.4.2 Radial drift

Small dust particles of $\sim 1\mu$m are well coupled to the gas in protoplanetary disks, and are supported by the gas pressure. As the particles grow to sizes $a \gg 1\mu$m their surface-to-mass ratio decreases and the dust particles dynamically decouple from the gas. If particles get bigger than their mean free path through the gas they will feel a friction when moving through it. Due to its radial pressure gradient, the gas orbits at sub-Keplerian velocity while large dust grains move almost at Keplerian velocities. This friction will create a drag force of the form

$$F_D = -\frac{1}{2} C_D \pi a^2 \rho_g v^2 \tag{1.13}$$

where πa^2 is the cross-section of the dust grain, ρ_g is the gas density, v is the relative velocity between the gas and the dust and C_D is the drag coefficient that depends on v and the relative size of the dust grain with respect to the mean free path of the gas. The drag force induced by the sub-Keplerian gas disk removes angular momentum from the dust particles and slows them down. This translates into a headwind that moves the decoupled dust particles inward. The drift velocity depends on the gas pressure gradient because it is what causes the gas to move at sub-Keplerian velocities (Nakagawa et al. 1986; Weidenschilling 1977).

A useful dimensionless parameter is the Stokes number (S_t) defined as

$$S_t = \Omega_K \tau_S, \tag{1.14}$$

where $\tau_S = mv/F_D$ is the stopping or friction time of a particle with mass m and velocity v due to drag forces (F_D) and Ω_K is the Keplerian angular velocity. Particles with the same Stokes number have identical aerodynamical behavior. Small particles with $S_t << 1$ will adapt to the gas velocity on shorter timescales than the orbital time scale. Similarly, big particles with $S_t >> 1$ will adapt to the gas velocity at much longer timescales than the orbital time scale. In the regime where $S_t < 1$ the radial velocity satisfies $v_r \simeq -2S_t \eta V_K$, which means that small particles drift inwards at lower velocities than larger particles.

Observational evidence of radial drift can be found by comparing the millimeter continuum emission in resolved disks, which roughly traces the distribution of mm-sized dust grains, to the extent of the molecular gas usually traced by CO (Panić et al. 2009). Protoplanetary disks usually exhibit a larger radial extent of their gas content, traced by CO, than that of the mm-sized dust grains, traced by the millimeter continuum. Although this difference can be explained as a consequence of optically thick CO emission (Hughes et al. 2008), detailed modeling of optically thin CO isotopes and (sub)millimeter continuum has shown that, for some disks, radial drift is a natural explanation of the difference in the radial extent of CO and continuum emission (Andrews et al. 2012; Isella et al. 2016). Moreover, it is the sharp steepening of the mm-sized grain distribution, rather than its smaller radial size, that is truly characteristic of radial drift.

1.4.3 Settling

In addition to drag forces, large grains of dust will experience a vertical gravitational force. For small vertical displacements ($z \ll r$) we can write this force as

$$F_g = -m\Omega_K^2 z. \tag{1.15}$$

By equating the vertical component of the stellar gravity to the drag force an expression for the settling time scale can be obtained

$$\tau_{\text{settling}} = (S_t \Omega_K)^{-1}. \tag{1.16}$$

For small particles ($a \ll 0.1\mu m$) this settling time will always be much larger than the orbital time, $\tau_{\text{orbit}} = \Omega_K$. The time scale for radial drift is much shorter, about 100 years for m-sized particles, than the time scale for dust settling, which is about 10^5 years. We can therefore consider that all grains that have settled have also migrated inwards. However, a fraction of the dust grains may not stay permanently settled since turbulent velocities produce vertical stirring and mixing of small particles (Dullemond & Dominik 2004b, 2005, 2008; Birnstiel et al. 2016).

1.4.4 Mixing

The gas evolution within the disk is thought to be driven by viscous accretion. The viscous nature of the gas will induce random motions in the dust that will act as a mixing mechanism on the dust. Just like vertical settling and radial drift, the mixing process is dependent on the size of the dust particles. A useful number is the Schmidt number, the ratio of dust diffusivity to gas diffusivity, defined as (Youdin & Lithwick 2007)

$$S_c = \frac{D_g}{D_d} \simeq 1 + S_t^2, \tag{1.17}$$

where it is usually assumed that the diffusivity of the gas equals its viscosity (Pavlyuchenkov & Dullemond 2007). This ratio is high for large particles and low for small particles, consistent with the notion of larger particles suffering less diffusion than small particles due to gas motions. This mixing results in the smoothing of the concentration of small dust grains and gas.

1.5 Disk chemistry

So far we have only discussed the physical structures and dynamical processes of protoplanetary disks. The large range of physical conditions throughout the disk implies an equally diverse chemistry produced by reactions ranging from photo-processes in the hot and irradiated regions to grain chemistry in the cold and dense disk. Because the disk temperature decreases with radius, we can roughly divide the chemistry into two regions: the inner warm disk at r$\lesssim$ 20 AU and the outer cold disk at larger radii.

The inner disk hosts a high temperature environment at 100-5000 K with densities as high as 10^{12} cm^{-3}. The dense midplane regions of the inner disk are shielded from high-energy ionization sources and the chemistry is driven by 3-body neutral-neutral reactions (Harada et al. 2010; Aikawa et al. 1999), such as the formation of molecular hydrogen. Chemical models predict a high abundance of H_2O, CO, NH_3, HCN and simple hydrocarbons, being destroyed only at very high temperatures by thermal dissociation (Willacy & Millar 1998; Markwick et al. 2002; Ilgner et al. 2004; Woods & Willacy 2007; Agúndez et al. 2008; Bethell & Bergin 2009; Najita et al. 2011; Walsh et al. 2015).

In the outer cold disk high-energy radiation and cosmic rays drive the chemistry of the disk dominated by ion-molecule reactions (Aikawa et al. 2002; van Zadelhoff et al. 2003; Gorti & Hollenbach 2004; van Dishoeck et al. 2006; van Dishoeck 2006; Fogel et al. 2011; Vasyunin et al. 2011; Walsh et al. 2012; Akimkin et al. 2013). Section 1.2.4 discusses the vertical gradient of the gas and dust temperature which is determined by the heating and cooling of the gas and dust triggered by the irradiation of the central star. The vertical positive gradient coupled with the UV radiation field result in three characteristic chemical regimes (Aikawa et al. 2002). Figure 7.1 shows a cartoon of these three regions: a cold chemistry region in the midplane dominated by surface processes in icy mantles, a rich warm molecular region where gas chemistry is active, and a restricted photon-dominated surface region where UV radiation dissociates and ionizes molecules driving an ion-molecule chemistry.

The cold outer midplane has temperatures below ~20-50 K with most of the molecules frozen out (with the exception of H_2) and hydrogenation reactions on the surfaces of the grains dominating the chemistry. The only ionization sources in these dense and cold region are cosmic ray particles and the secondary UV photons they produce. Molecules like CO, N_2 and simple hydrocarbons evaporate at temperatures around ~ 20 K. The local

UV radiation field might also contribute to the release of icy molecules to the gas-phase in cold environments through photodesorption.

Gas-phase chemistry in the intermediate warm molecular layer is dominated by ion-molecule processes, such as proton transfer from species like H_3^+ (Herbst & Klemperer 1973; Watson 1974; Woodall et al. 2007; Wakelam et al. 2012). This region is only partially shielded from high-energy radiation and temperatures are high enough, even at large radii, for molecules such as CO and N_2 to evaporate from icy dust grains. Water has a higher sublimation temperature, around 170 K (Hayashi 1981) dependent on the pressure, and thus remains mostly frozen-out. The location of this temperature threshold is commonly known as the molecule's snowline, to refer to its radial location in the midplane, or snow surface, since the vertical temperature structure of the disk will define an isothermal surface across the radial axis.

This snowline is a function of the luminosity of the central star and the evolutionary stage of the disk. The water snowline likely moves inward from larger radii in the early hotter embedded phase (Kennedy & Kenyon 2008; Zhang & Jin 2015). Additionally, protostellar outbursts can abruptly heat the disk moving its location (e.g. Cieza et al. 2016). The water snowline is difficult to probe because is usually to close to the central star. The CO snowline, that occurs at around ~20 K, is further out at a few tens of AU. It has been indirectly imaged through chemical tracers in a couple of disks (e.g. Qi et al. 2013, 2015; Mathews et al. 2013).

The upper region in the disk atmosphere is dominated by the stellar UV radiation and the interstellar radiation that ionizes and dissociates molecules. These processes depend

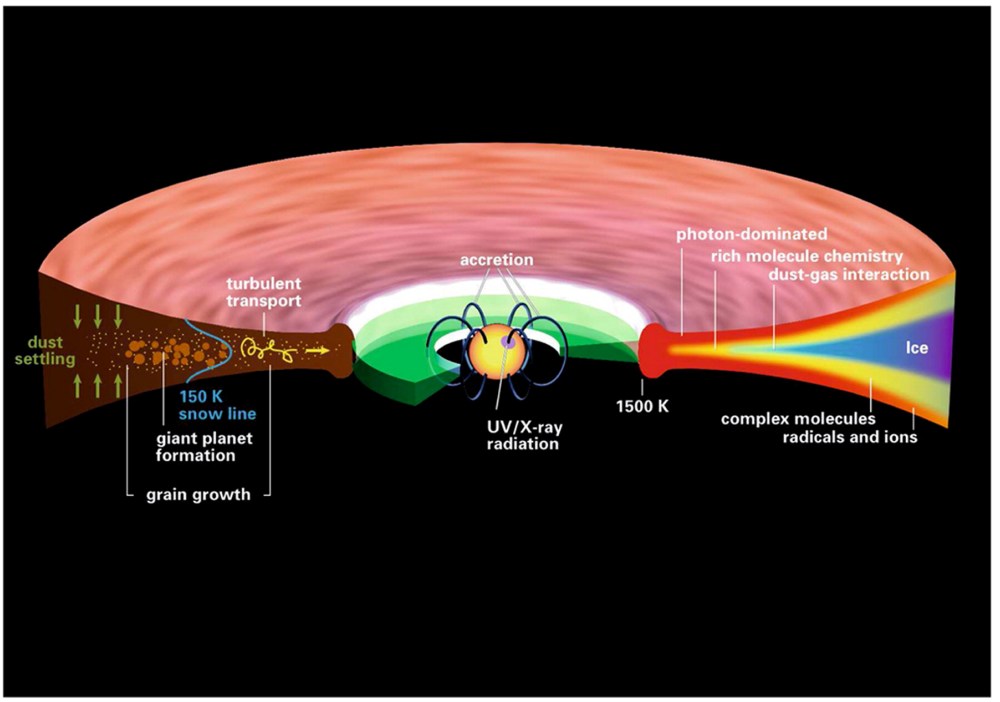

Figure 1.3: Cartoon of dust evolution and chemical regions in the disk. Taken from Henning & Semenov (2013).

strongly on the shape and intensity of the high-energy radiation field. For example, Lyman α photons will dissociate HCN and H_2O, while other molecules such as CO and H_2 are protected by self-shielding and mutual shielding (van Dishoeck & Black 1988; van Dishoeck et al. 2006; Heays et al. 2017).

1.5.1 Material inventory

Gas

To construct an inventory of chemical species high spectral resolution is needed. Disks are optically thick at IR wavelengths and emission lines can only be seen from the upper warm layers, but the disk is mostly optically thin in the (sub)millimeter regime and there we can trace molecular lines throughout the entire disk. Figure 1.4 shows a schematic summary of the main molecular diagnostic of disks.

A large body of observational work has provided an inventory of the molecular content of disks (e.g. Dutrey et al. 1997; Thi et al. 2004; Schreyer et al. 2008; Henning et al. 2010; Öberg et al. 2010, 2011b,c, 2015; Dutrey et al. 2011; Chapillon et al. 2012a,b). Molecules such as CO, HCN, HCO^+, H_2O and recently the complex organic CH_3OH (Walsh et al. 2016) have been found toward protoplanetary disks. Their line intensities can be transformed to abundances if a density and temperature is provided. One of the most important results of this work is the depletion of molecules in comparison with ISM abundances due to low temperatures (freeze out) or photodissociation within the disk (Kastner et al. 1997; Dutrey et al. 1997; van Zadelhoff et al. 2001).

In the Far-IR regime, the PACS and HIFI instruments aboard *Herschel* have detected higher rotational transitions of CO, that account for gas at $T \sim 100 - 1000$ K, hydroxyl,

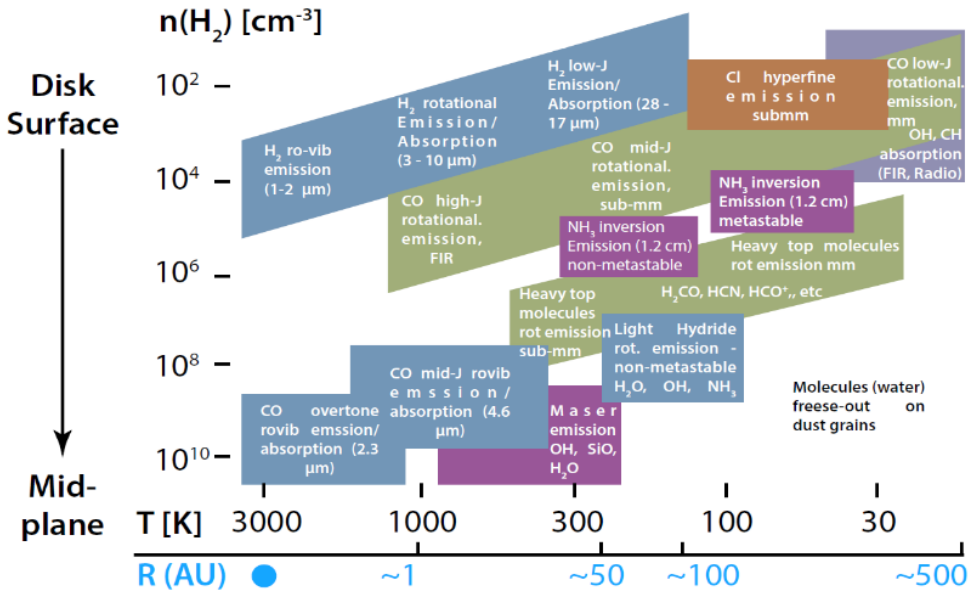

Figure 1.4: Schematic representation of the radial and vertical locations in a disk where molecular species are expected to dominate the line emission taken from Dionatos (2015) based on Genzel (1992).

water, atomic oxygen and CH^+ toward several protoplanetary disks (Fedele et al. 2012; Meeus et al. 2012; Riviere-Marichalar et al. 2012; Fedele et al. 2013; Hogerheijde et al. 2011; Sturm et al. 2010; Meeus et al. 2013). In the mid- and near-IR regimes, *Spitzer* and ground-base telescopes provided a forest of H_2O and OH line in many disks, along with CO, and organic molecules such as HCN and C_2H_2 (Lahuis et al. 2006; Carr & Najita 2008; Salyk et al. 2008; Pascucci et al. 2009; Pontoppidan et al. 2010; Carr & Najita 2011; Salyk et al. 2011; Mandell et al. 2012).

Ice

The major components of astronomical ices, such as H_2O, CO, CO_2, CH_4, CH_3OH, NH_3 and HCOOH, have been detected through their IR features toward embedded protostar and background stars (van Dishoeck 2004; Gibb et al. 2004; Whittet et al. 2007; Boogert et al. 2015). The icy mantles grow by accretion of atoms and molecules from the gas where molecules like CO_2, H_2CO and CH_3OH are formed through atom addition reactions, CO and O_2 (van de Hulst 1946; Watson 1976; Ioppolo et al. 2008; Miyauchi et al. 2008; Dulieu et al. 2010). A rich surface chemistry, even at low temperatures of $\sim$ 10 K, forms more complex molecules (e.g. Fedoseev et al. 2017) and these are subsequently processed by high energy photons and cosmic rays present in the ISM (Benz et al. 2010; Bernstein et al. 1995; Moore & Hudson 1998; Bennett et al. 2005). In the high temperature environments of massive and low-mass protostars, these icy mantels sublimate. In these so-called hot cores and hot corinos, major ice species as well as minor constituents, like some complex organics and nitrogen-bearing species, return to the gas where they can be easily identified through rotational gas-phase spectroscopy (Herbst & van Dishoeck 2009).

Some of this icy reservoir is reprocessed in the early stages of protoplanetary disks through thermal desorption followed by gas chemistry. They are ultimately frozen out again in the outer colder region of the disk where they potentially mix with pristine ices still present there (Caselli & Ceccarelli 2012; Brownlee 2014; Cleeves et al. 2014; Furuya & Aikawa 2014). Models by Visser (2009) suggest that most of the material that ends up in the comet-forming region experiences a large degree of chemical reprocessing, a result supported by the cristallinity fraction found in solar system comets. However, at the same time, comets also contain material very similar to young protostars. Comets may have mixed material from both pristine regions in the outer parts of the disk and from heavily reprocessed regions.

The freeze-out time scale t_{freeze} for the standard gas-to-dust mass ratio of 100 and a sticking probability of 1 can be roughly estimated by the following expression

$$t_{\rm freeze} \approx \frac{10^9 {\rm cm}^{-3}}{n_{\rm H}} \frac{a}{0.1 \mu{\rm m}} {\rm yrs} \tag{1.18}$$

where $n_{\rm H}$ is the gas particle density (in cm^{-3}) and a is the typical grain radius (in μm). The freeze-out time scales in the cold midplanes of protoplanetary disks (with typical densities of $\sim 10^6$–10^8 cm^{-3}) are of the order of 10–10^3 years, indicating that most of the material in the gas phase is frozen-out within a tiny fraction of the disk lifetime.

The most important desorption process for volatiles such as CO, N_2, and CH_4 is thermal desorption. In regions where UV radiation can penetrate, photodesorption of these ices also becomes important. Additionally, cosmic ray and X-ray spot heating may release mantle material back to the gas phase in cold regions deep in the midplane (Leger et al. 1985; Hasegawa & Herbst 1993; Najita et al. 2001). The photodesorption rates of CO, H_2O, CH_4, and NH_3 have recently been derived experimentally (Öberg et al. 2007; Öberg 2009; Öberg

et al. 2009a,b; Fayolle et al. 2011; Cruz-Diaz et al. 2012; Fedoseev et al. 2015). Observations of NH_3 in ices suggest that it is usually intermixed with H_2O on interstellar ices (Merrill et al. 1976; Knacke et al. 1982; Smith et al. 1989; Bottinelli et al. 2010). Chemical models of protoplanetary disks show that photodesorption by UV radiation significantly affects molecular column densities of the most abundant molecules such as HCN, CS, H_2O, NH_3 and CO_2 (Willacy 2007; Semenov & Wiebe 2011; Walsh et al. 2010).

Dust evolution processes and the intrinsic characteristics of the physical structure of disks drive the subsequent reprocessing of some of these species by changing the penetration of UV photons. This thesis explores the interrelationship between the dust, the temperature structure and the chemistry driving the formation of observable molecules. In particular, it explores the link between the location of the main oxygen- and nitrogen-bearing species (H_2O and NH_3) and the mm-sized dust particle distribution.

1.5.2 Water

Water was detected in the ISM more than 40 years ago (Cheung et al. 1969) and, subsequently in vapor and ice form, toward a number of YSOs and protoplanetary disks (Gillett & Forrest 1973; Cernicharo & Crovisier 2005; Boogert et al. 2008; Melnick 2009; Hogerheijde et al. 2011; Bergin & van Dishoeck 2012). Water is the most abundant volatile in interstellar and cometary ices (see reviews by Mumma & Charnley 2011; Boogert et al. 2015). At temperatures higher than 230 K water is the dominant gas-phase oxygen carrier. It forms through neutral-neutral reactions of $O+H_2 \rightarrow OH+H$ followed by $OH+H_2 \rightarrow H_2O+H$ (Elitzur & Watson 1978; Atkinson et al. 2004). At temperatures below 100 K water forms through ion-neutral reaction and dissociative reactions. It starts with $H_3^+ + O \rightarrow H_2 + OH^+$ followed by a series of reactions of OH^+ or H_2O^+ with H_2, leading to H_3O^+ that is finally recombined to H_2O+H (Herbst & Klemperer 1973). In addition, H_2O can form on grains surfaces through hydrogenation of O, O_2 and O_3. The whole chemical network involves photo-dissociation, photo-desorption and freeze-out summarized in Fig.1.5 (see van Dishoeck et al. 2014, and references therein). Water ice is known to be frozen out already in pre-stellar and protostellar phases and it is only thermally evaporated in the disk within $\sim$ 10 AU from the star.

1.5.3 Ammonia

NH_3 was one of the first molecules identified in the ISM (Cheung et al. 1968) and is readily detected in star forming regions (Morris et al. 1973; Irvine et al. 1987; Persson et al. 2010; Bottinelli et al. 2010; Daranlot et al. 2012). In disks, detailed chemical models have shown ammonia to form as a product of warm gas-phase reactions and ion-molecule reactions (see Fig. 1.6). On grains, ammonia forms through atomic nitrogen hydrogenation (Brown & Millar 1989; Fedoseev et al. 2015). About 10%-20% of nitrogen is contained in ices such as NH_3, NH_4^+, and XCN, the latter mostly in the form of OCN^- (Öberg et al. 2011a). Processes to release NH_3 from ice to gas, at temperatures below the thermal desorption, include cosmic-ray desorption (Hasegawa & Herbst 1993), reactive desorption (Garrod et al. 2007) and photodesorption (Prasad & Tarafdar 1983). This process dominates during the very early stages of star formation. In more evolved stages, where protoplanetary disks are formed, the bulk of ammonia is locked in the ice and gas-phase formation is the only process left active (Sipilä et al. 2015; Harju et al. 2017). This process occurs through a well-known chain of reactions, starting with the dissociation of N_2 (by photo-processes or He^+) and terminating in $NH_4^+ + e \rightarrow NH_3 + H$ (Le Gal et al. 2014; Roueff et al. 2015; Walsh et al. 2014).

1.5.4 Deuterium chemistry in Disks

The initial cosmic elemental D/H fraction, produced in the Big Bang, was $\sim 2.5 \times 10^{-5}$ (Cooke et al. 2016). In present days the D/H ratio in the cold ISM is $\sim 2.0 \times 10^{-5}$ (Prodanović et al. 2010). The D/H ratio of H_2 in the solar surroundings is similar to that of the diffuse ISM. Simple molecular species, such as DCO^+, DCN and HDCO, have D/H ratios that are higher than the cosmic and cold ISM values by two order of magnitude (Roberts et al. 2002; Bacmann et al. 2003; Vastel et al. 2006). The temperature of the regions where key molecular species, present in protoplanetary disks and solar system bodies, were formed (or processed) can be traced by measuring their D/H ratio. The high deuterium fractionation at low temperatures is a consequence of the lower zero-point vibrational energy of simple deuterated molecules in comparison to their non-deuterated counterparts (Combes et al. 1985; Millar et al. 1989; Turner 2001; Gerner et al. 2015). We can distinguish three main

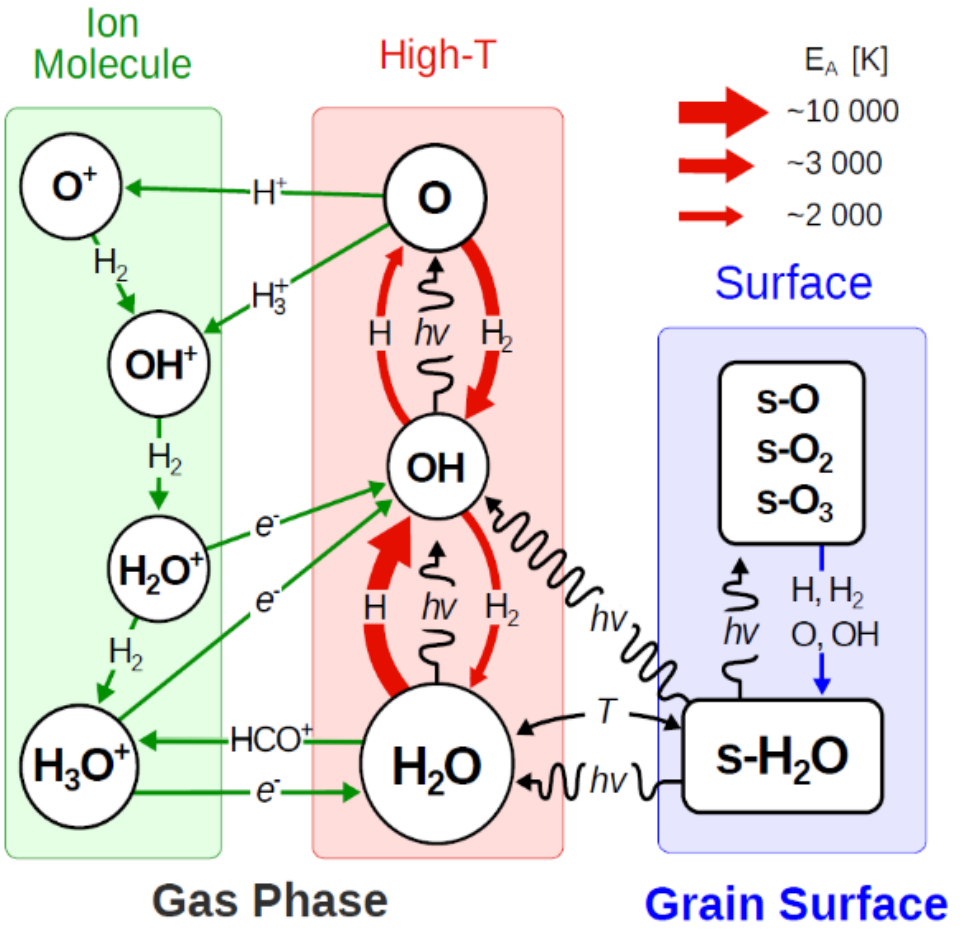

Figure 1.5: Summary of the main gas-phase and solid-state chemical reactions leading to the formation and destruction of H_2O. *e* stands for electron, *ν* for photon and s-X indicates that species X is on the grains. This figure was taken from (van Dishoeck et al. 2014).

reactions through which deuterium is injected into the chemistry,

$$H_3^+ + HD \leftrightharpoons H_2D^+ + H_2 + 230K, \tag{1.19a}$$

$$CH_3^+ + HD \leftrightharpoons CH_2D^+ + H_2 + 370K, \tag{1.19b}$$

$$C_2H_2^+ + HD \leftrightharpoons C_2HD^+ + H_2 + 550K. \tag{1.19c}$$

Equation 1.19a is preceded by cosmic ray ionization of H_2 producing the H_3^+ ion. The left-to-right reaction of Eq. 1.19a is exothermic and strongly enhances the D/H ratio of H_2D^+, and species that derive from it, at temperatures below ~30 K (Millar et al. 1989; Albertsson et al. 2013). This regime corresponds to the so-called low temperature deuteration channel. In contrast, the left-to-right reactions of Eq. 1.19b and 1.19c, involving light hydrocarbons, effectively enhance the deuterium fractionation at higher temperatures than Eq. 1.19a but below ~ 80 K. This regime corresponds to the high temperature deuteration channel. Deuterium fractionation initiated by the H_2D^+ is particularly effective at low temperatures in disk midplanes. In these regions CO is frozen out, otherwise it would react with H_3^+ before HD. Similarly, at low temperatures, grain surface reactions may also contribute enhance the D/H molecular ratio of selected species (Tielens 1983).Recently it was realized that the ortho-to-para ratio of molecular H_2 can hinder the deuterium enhancement because of the differences in internal energies of o-H_2 and p-H_2 (Flower et al. 2006; Pagani et al. 2009). The reverse endothermic reactions of Eq. 1.19a, 1.19b and 1.19c proceed more rapidily for the reaction involving o-H_2 than the corresponding reaction involving p-H_2.

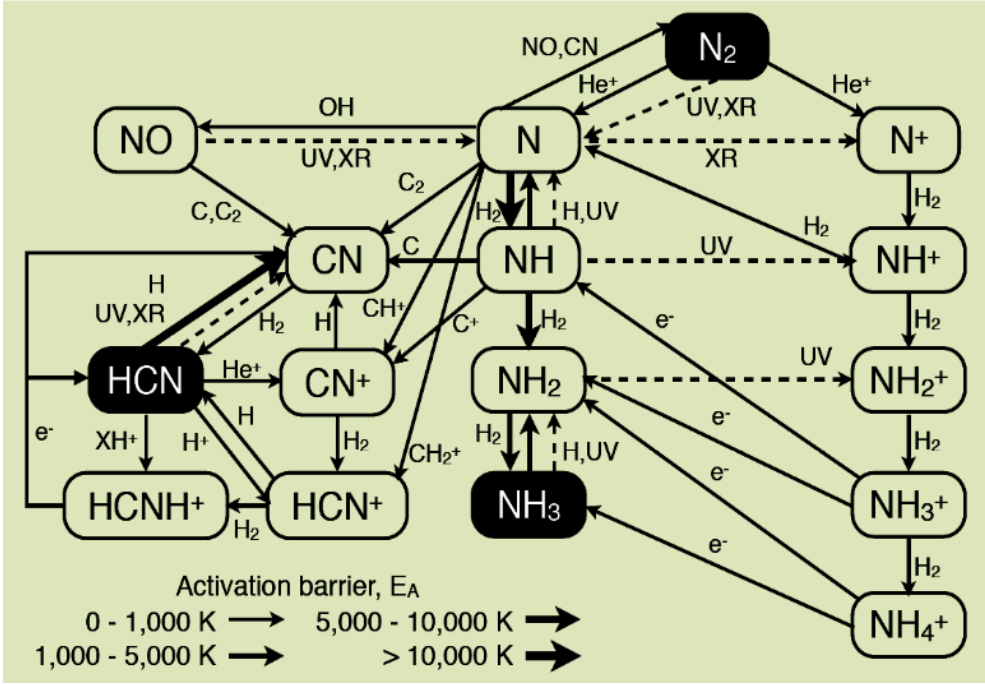

Figure 1.6: Schematic chemical network of the main gas-phase processes that involve NH_3, taken from Walsh et al. (2015).

Cold ISM regions show D/H molecular ratios a factor of 100-300 higher than the elemental D/H (Roberts et al. 2002; Bacmann et al. 2003; Vastel et al. 2006). In contrast, the D/H molecular ratios found in meteorites and comets from the Oort cloud are a factor of 10-30 higher than the elemental D/H ratio (Irvine et al. 2000), but about an order of magnitude lower than in the cold ISM. The D/H ratio in Earth can be probed by measuring the HDO/H_2O ratio of about $\sim 1.6 \times 10^{-4}$, consistent with the idea of a dry proto-Earth that got most of its oceans from asteroids as opossed to long-period comets in the last phase of its formation (Morbidelli et al. 2000). Long period comets have a water deuterium enrichment a factor of two higher than that of Earth, suggesting that the bulk of Earth's water was delivered at early stages through massive planetary embryos, with lower HDO/H_2O ratios, in the asteroid belt. Chemical models, including a comprehensive treatment of disk ionization, show that the ion-driven deuterium pathways are inefficient to explain the observed enriched HDO/H_2O ratio of solar system bodies (Cleeves et al. 2014), implying that a considerable fraction of the water reservoir of the solar nebula was inherited from the ISM.

Other detuerated molecules, such as DCN and DCO^+, have been detected toward protoplanetary disks. The D/H ratios of DCN and DCO^+ in TW Hya (Öberg et al. 2012) are much higher than elemental D/H ratios, by several orders of magnitude. DCN is more centrally peaked than DCO^+, suggesting different fractionation pathways. DCN is believed to be formed mainly through Eq. 1.19b while DCO^+ is thought to form through Eq. 1.19a. However, recent chemical models have proposed reactions involving Eq. 1.19b and 1.19c leading to production of DCO^+ at higher temperatures than Eq.1.19a (Favre et al. 2015).

1.6 Methods

1.6.1 Observations

This thesis makes use of the available data from the HIFI instrument aboard the *Herschel Space Telescope* in the far-IR regime and the Atacama Large Millimeter/submillimeter Array (ALMA) in the (sub)millimeter regime toward two disks. *Herschel* had a 3.5 m single mirror and operated between 2009 and 2013. It carried three detectors: the Photodetector Array Camera and Spectrometer (PACS) (Poglitsch et al. 2010), covering wavelengths from 55 to 210 μm; SPIRE (Griffin et al. 2010), an imaging camera covering wavelengths from 194 to 672 μm; and HIFI (de Graauw et al. 2010) an heterodyne detector operating in two wavelengths bands from 157 to 212 and 240 to 625 μm. At these wavelengths, the primary beam size is 11"-19" and 21"-43", respectively. The *Herschel* beam cannot provide resolved spatial information of protoplanetary disks but it is capable of observing the far-IR regime that hosts several interesting molecular and atomic transitions only attainable from space. The HIFI instrument has very high spectral resolution, which can be used for reasonable inclined disks to pinpoint the location of the emission.

The guaranteed-time *Herschel* key programme "Water In Star-forming regions with Herschel" (WISH van Dishoeck et al. 2011) observed fundamental water rotational transitions and high-J CO transitions with unprecedented spectral resolution toward sources related to star formation including several protoplanetary disks using HIFI and PACS. *Herschel* provided unique spectral coverage and sensitivity, unmatched by earlier missions and not surpassed in the near future. The far-IR regime, probed by the HIFI instrument, hosts unique ground level transitions of key molecules in disks, such as NH_3 and H_2O. This thesis analyses *Herschel* HIFI data in relation to the resolved millimeter continuum emission (from ALMA) to provide constraints on the amount of volatile water and ammonia, and the

mechanisms responsible for their release in the gas phase.

ALMA is an interferometric facility of sixty-six 12 m and 7 m radio telescopes at ∼ 5000 m of altitude in the Chilean Andes. Compared to the modest eight antennas of 6 m of the SMA, ALMA is a huge improvement for the observation of the cold universe in the (sub)millimeter regime. The ambitious set up of ALMA allows it to reach spatial resolutions of a few milli-arcseconds for its most extended configuration and spectral resolutions better than ∼ 0.05 km s^{-1}. The (sub)millimeter regime probed by ALMA has many rotational transitions of simple (e.g. CO) and complex (e.g. CH_3OH) molecules that give valuable information of the gas dynamical and chemical processes occurring in planet-forming disks.

The analysis of interferometric data is best done in the *uv*-space. The *uv*-space is the Fourier space of the coordinates (x, y) in the sky. Interferometers measure the interference pattern, or visibilities, of the image plane in a discrete sample of the *uv*-space defined by the available baselines. An interferometer has as many baselines as permutations of pairs of its antennas. The resolution of a particular set of baselines (B) is given by $\lambda/B_{\rm max}$, where λ is the observed wavelength and $B_{\rm max}$ is the longest available baseline. Because of this relationship, baselines are usually given in kλ rather than the standard SI units.

In the pre-ALMA era most of the spatially resolved observations of disks in the millimeter regime were obtained with interferometric arrays such as the PdBI, CARMA and SMA to a resolution of about 0.5-1″. In addition to molecular transitions, several resolved millimeter images of disks showed ring-like structures (Piétu et al. 2006; Brown et al. 2009; Andrews et al. 2011; Williams & Cieza 2011). These structures where modeled in the Fourier space

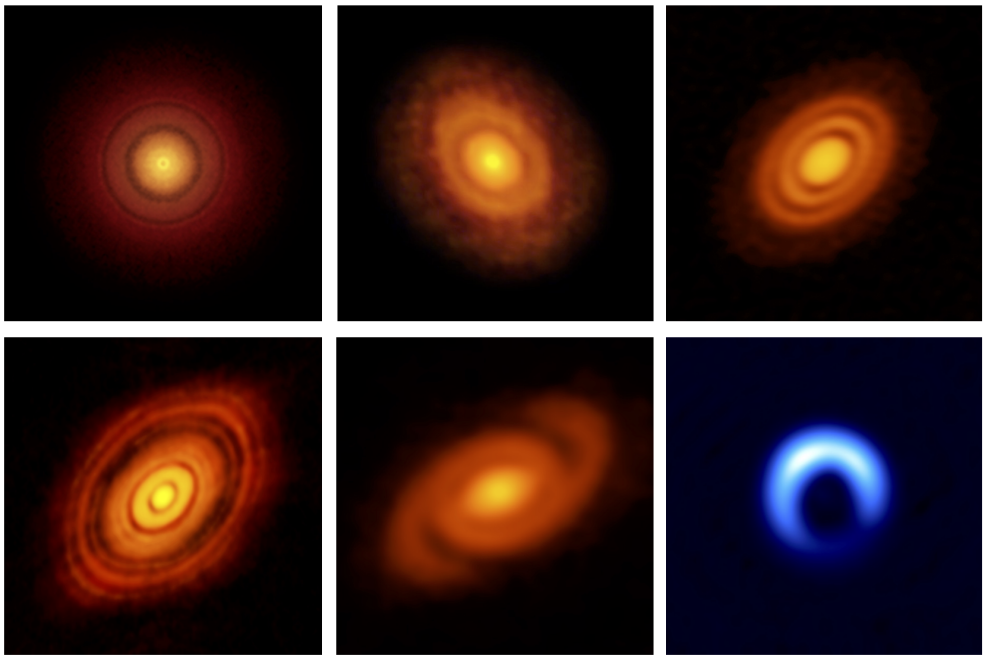

Figure 1.7: Gallery of high angular resolution continuum observations of planet forming disks obtained with ALMA. From left to right and from top to bottom: TW Hya (Andrews et al. 2016), V883 Ori (Cieza et al. 2016), HD163296 (Isella et al. 2016), HL Tau (ALMA Partnership et al. 2015), Elias 2-27 (Pérez et al. 2016), HD142527 (Kataoka et al. 2016). Credits: S. Andrews, L. Cieza, A. Isella, A. Kataoka, B. Saxton (NRAO/AUI/NSF), and ALMA (ESO/NAOJ/NRAO).

with simple parametric models but the modest *uv*-coverage and low sensitivity made the disentanglement of several degenerate disk models difficult (Andrews et al. 2009, 2010; Isella et al. 2009). ALMA has already reached an unprecedented spatial resolution (see Fig. 1.7) and has revealed substructures, in the continuum emission of disks, that can trace various dust evolution processes. This thesis will use both molecular and continuum observations taken with ALMA to determine the formation origin of simple deuterated molecules.

1.6.2 Modeling

Each of the chapters in this thesis analyses molecular transitions obtained with the instruments presented in the previous section. The general methodology to model them includes first the adoption of pre-existent physical models from the literature. These models are obtained by fitting the SED with a parametric model of the dust surface density and a temperature profile calculated self-consistently with radiative transfer codes. The observed molecular lines are then interpreted using abundance models to calculate their resulting line emission that are either parametric or follow from detailed chemical calculations. The line radiative transfer is performed using the 3D radiative transfer code Line Modeling Engine (LIME) capable of calculating the population levels out of local thermodynamical equilibtrium (LTE). In LTE the population of the molecular energy states is given by a Boltzmann distribution of the form

$$\frac{n_u}{n_l} = \exp\left(-\frac{E_u - E_l}{k_B T_{\rm K}}\right) \tag{1.20}$$

where $T_{\rm K}$ is the kinetic temperature of the gas and k_B is the Boltzmann constant. In non-LTE the population energy levels are calculated by solving the population number of the levels in statistical equilibrium

$$\frac{\partial n_u}{\partial t} = -n_u(A_{ul} + B_{ul}\bar{J} + C_{ul}) + n_l(B_{lu}\bar{J} + C_{lu}) = 0 \tag{1.21}$$

where A_{ul} and B_{ul} are the Einstein coefficients, C_{ul} are the collisional rates and $\bar{J}$ is the line profile integrated mean intensity. The first term accounts for spontaneous emission, induced emission and collisional de-excitation and the second term for absorption and collisional excitation, respectively. We can define an excitation temperature ($T_{\rm ex}$) for the molecular transition calculating the population ratio of the upper and lower energy levels as $n_u/n_l = \exp(-(E_u - E_l)/k_B T_{\rm ex})$. In the limit where the density of the collisional partner exceeds a critical density, defined as $n_{\rm crit} = A_{ul}/C_{ul}$, collisions drive the excitation to LTE and we recover the LTE distribution of Eq. 1.20 with $T_{\rm ex} = T_{\rm K}$. The following sections briefly describe the radiative transfer codes used in this thesis.

Physical models

The TORUS code (Pinte et al. 2009; Harries et al. 2004; Harries 2000) is a Monte Carlo radiative transfer code in 3D that fully treats polarization and multiple scattering. It can use either Mie or Rayleigh scattering. The temperatures are computed treating the dust in local thermodynamic equilibrium being only heated by stellar radiation. Radiative equilibrium is computed using the continuous absorption algorithm from Lucy (1999). All the calculations are performed on a cylindrical adaptive-mesh in 2D. The temperature structure is computed with a diffusion approximation method.

The RADMC code (Dullemond & Dominik 2004a) is a Monte Carlo continuum axisymmetric 3D radiative transfer code. It employs the algorithm from Bjorkman & Wood (2001)

but with a continuous treatment of energy instead of the discrete original one. The radiation is propagated using isotropic scattering , unlike the TORUS code that performs anisotropic scattering, and it computes the dust temperature.

Radiative transfer (LIME)

LIME is a non-LTE radiation transfer code for (sub)millimeter, far-IR continuum and spectral lines, that has the advantage of working with an arbitrary 3D geometry faster than other radiative transfer codes. It was developed by Christian Brinch (Brinch 2008; Brinch & Hogerheijde 2010) as a derivation from the RATRAN code (Hogerheijde & van der Tak 2000). Whereas RATRAN uses a Cartesian grid, LIME uses a random grid that adapts to the provided density structure or other aspects of interest (e.g. the molecular abundances). After the points have been chosen LIME constructs a Delaunay triangulation (Barber et al. 1996) and its corresponding Voronoi tessellation that define the cells that are represented by the physical properties of the grid points.

LIME requires the rate coefficients of the line transitions and dust opacities as separate inputs. Troughout this thesis the Einstien A_{ul} and collisional C_{ul} coefficients are taken from the LAMBDA database (Schöier et al. 2005). The opacities are taken from Ossenkopf & Henning (1994) for a standard dust size grain distribution.

1.7 This thesis

1.7.1 Aim

The rapid advance of observational techniques has unveiled very rich and complex structures in protoplanetary disks. The arrival of ALMA revealed exquisite substructure in the mm-grain distribution (e.g. Zhang et al. 2016; Isella et al. 2016; ALMA Partnership et al. 2015) and in molecular emission (e.g. Qi et al. 2015; Carney et al. 2017; Öberg et al. 2015). This makes ALMA an excellent instrument to explore the impact of the radial and vertical distributions of mm-sized dust into the distribution of molecules and their formation pathways. This thesis aims to understand the processes and formation origins that shape the structures and distributions seen in major nitrogen, oxygen and carbon species by contrasting them with the structures produced by dust evolution, photo-processes and gas-phase chemistry. Specifically we aim to answer two questions: **what is the spatial distribution of the main oxygen- and nitrogen-bearing species in planet-forming disks as probed by water and ammonia?** and **what is the relationship between physical features, such as the location of the CO snowline and substructures of temperature and the distribution of large dust grains, and the formation and chemistry of common molecular species?**

To this end we focus on two case studies: the disks surrounding TW Hya, a T Tauri star, and HD163296, a Herbig Ae star. Their high disk mass and proximity makes them excellent laboratories to explore the structure of the dust and simple molecules. These disks have been widely studied and modeled in past literature. TW Hya is a close (56 pc van Leeuwen 2007) low-mass star (~ 0.8 $M_\odot$) hosting a disk of mass $\sim$0.04 $M_\odot$ (Cleeves et al. 2014; Bergin et al. 2013; Webb et al. 1999). It is estimated from stellar evolutionary tracks to be between 8-10 Myr old (Hoff et al. 1998; Webb et al. 1999; de la Reza et al. 2006; Debes et al. 2013) with some uncertanties depending on the assumed stellar type (Vacca & Sandell 2011). The TW Hya disk is almost face on (7°) and its gas content extends radially to $\sim$200 AU (Qi et al. 2004). The Herbig Ae star HD163296 is an intermediate-mass star (2.3 $M_\odot$) at 122 pc (Perryman et al. 1997) surrounded by a disk with a mass of $\sim$ 0.09 $M_\odot$ (Qi et al. 2011).

Unlike TW Hya, it is inclined by 44° and its gas content extends up to 500 AU in radius (Mathews et al. 2013). This thesis uses data from the HIFI instrument on board *Herschel* and ALMA data of molecular lines and millimeter continuum toward these sources.

In **Chapter 2** we use ALMA Band 7 continuum data at 820 μm of TW Hya to fit a model of the surface density to probe the mm-sized dust radial distribution. The interferometric visibilities are described by a model with a broken power law with slopes of -0.57 and -8.0 and a turn-over radius of ~47 AU. This is consistent with the expected shape of the surface distribution in the presence of grain growth and radial migration (Birnstiel & Andrews 2014). However, the derived turn-over radius and the total surface brightness are too large for a disk of 8-10 Myr. This could be reconciled considering a much larger initial disk size and disk mass, a gap halting the inward radial drift opened by an unseen embedded planet or a locally enhanced production rate of mm-sized grains due to the higher sticking efficiency of icy grains in the region outside the CO snowline.

In **Chapter 3**, the detection of the o-NH_3 $1_0 - 0_0$ line with the HIFI instrument on board *Herschel* toward TW Hya is presented; the first ever toward a planet-forming disk. Together with past detections of the ground-state rotational lines of o-H_2O and p-H_2O towards the same source, this chapter explores the radial and vertical distribution of these species under the assumption that water and ammonia ices are intermixed and co-desorbing. Only a compact and settled distribution of gas-phase NH_3 and H_2O, following the millimeter continuum emission radial extent of $r \lesssim 60$ AU, is consistent with the NH_3/H_2O ratio of interstellar ices and solar system bodies of ~5%-10%. Additional gas-phase formation of NH_3 is needed to reconcile the observed emission with any other possible configuration. The total reservoir of water and ammonia in the disk is estimated to be about six orders of magnitude higher than the gas-phases masses of NH_3 and H_2O for any of the explored distributions indicating that the majority of these molecules are locked up in ices.

Chapter 4 continues to explore the spatial location of gas-phase NH_3, this time in the disk around HD163296. Both *Herschel* data of the o-NH_3 $1_0 - 0_0$ line and ALMA data of the p-NH_2D $1_0 - 0_0$ line result in non-detections, that still provide meaningful upper limits. Two radial distribution models of the distribution of these molecules are considered: one following the millimeter continuum emission at $r \lesssim 290$ AU, like the preferred TW Hya model from Chapter 3, and another one extending up to $r \lesssim 500$ AU, the full extent of the disk. The derived upper limits for the total mass of gas-phase o-NH_3 and p-NH_2D suggest that this disk is NH_3-poor, by a factor of 5 at least, compared to the similar-mass disk of TW Hya. Comparing other nitrogen-bearing species found in the literature toward these two disks indicates that this difference is due to the formation pathway of ammonia and not an overall lack of elemental nitrogen.

Chapter 5 focuses in the radial characterization of three simple deuterated species, DCO^+, DCN, and N_2D^+ detected with ALMA in Band 6 in the disk of HD163296. Assuming optically thin lines and LTE to convert line fluxes to column densities, the radial emission profile of the DCO^+, DCN and N_2D^+ lines is fitted using parametric abundance profiles. The DCO^+ radial emission profile is described by three consecutive radial regions with different constant abundances from ~50 AU to ~316 AU with two radial breaks at ~118 AU and ~245 AU. The best-fit models of the radial emission profiles of DCN and N_2D^+ correlate spatially with the first two radial regions of the best-fit model of DCO^+. We interpret this as an indication of the correlation of their chemical pathways; DCN and N_2D^+ form through the warm and cold deuteration channel, respectively, while DCO^+ is thought to form through both channels. The origin of the third DCO^+ radial region, from ~245 AU to ~316 AU, may trace a thermal inversion at large radii, a local decrease of the ortho-to-para ratio of H_2 or a decrease of the UV opacity due to grain growth.

Chapter 6 continues the analysis of the DCO^+ radial emission profile through simple chemical modelling of the cold deuteration channel and a parametric treatment of the warm deuteration channel in 2D. This simple chemical model coupled with a thermal inversion at $\sim$ 260 AU reproduces the third radial region identified in Chapter 5. Radial thermal inversions are predicted by theoretical models as a direct consequence of radial drift and settling of dust grains (Facchini et al. 2017).

1.7.2 Overall conclusions

The above summaries contain the specific conclusions drawn from the data and modelling of each chapter. This section presents the overall conclusions of this thesis aimed at answering the two questions posed in our initial goal (see Sec. 1.7.1). First, regarding the location of NH_3 and H_2O in planet forming disks we conclude that:

- Gas-phase NH_3 and H_2O in TW Hya emit from a compact and settled spatial configuration that follows the ice reservoir trapped in large bodies which is several orders of magnitude higher than the amount of gas-phase material. This means that the location of oxygen- and nitrogen-bearing volatiles in disks are set by grain evolution, in particular radial drift (Chapter 3).

- Additional spatially resolved observations of these molecules toward these planet-forming disks are crucial to confirm these scenarios. The deuterated isotopologues of NH_3 and H_2O are readily detected with ALMA in a few hours toward TW Hya and HD163296 (Chapters 3 & 4).

Second, regarding the effect of the physical structures on the distribution of simple molecules (and vice versa) we can conclude that:

- The spatial location of temperature-sensitive species, such as DCO^+, trace substructures in the temperature profile of protoplanetary disks and therefore (indirectly) the impact of dust evolution process on its morphology. Although to first order the temperature profile is determined by the disk's exposure to stellar radiation, dust grain evolution models show that settling and radial drift have an important role in creating substructures in the temperature profile (Chapters 5 & 6).

- The inverse process, namely how the location of simple molecules can impact dust evolution, can be studied by comparing the location of the snowline of main molecular species and the shape of the millimeter emission in planet-forming disks (Chapter 2).

1.7.3 Future outlook

ALMA has brought us impressively high spatial resolution images of protoplanetary disks these past six years. The recent effort to push its limits delivered an incredibly detailed image of a set of rings in the embedded disk around HL Tau as part of the Long Baseline Campaign (ALMA Partnership et al. 2015). Rich structures are hidden below the resolution of the observations presented in this thesis that affect the observed molecules. This is especially true for single-dish observation in the far-IR where no spatial information can be recovered. The high sensitivity and spatial resolution of ALMA can provide the means to disentangle both the distribution of key molecules, e.g. deuterated isotopologues of H_2O and NH_3, as well as the distribution of the millimeter-sized dust in the continuum. In addition,

multifrequency analysis of ALMA data can put a constraint on dust evolution indicators, such as the degree of dust growth toward planet-forming disks.

New mid and far infrared space facilities, with higher sensitivities than *Herschel*, will allow us to expand the detection sample of key carbon-, oxygen- and nitrogen-bearing species toward disks. So far key features of disks, such as the location of snowlines, the millimeter and infrared emission profile, and the distribution of main volatiles have been determined in a handful of disks with very different physical properties. This is in part due to the limited capabilities of the current instruments. Instruments like the mid-infrared MIRI instrument on board the future James Webb Space Telescope (JWST), the SMI on board the planned Space Infrared Telescope for Cosmology and Astrophysics (SPICA) and the Origins Space Telescope (OST) will be able to observe rotational and vibrational molecular transitions of key molecules such as HD, CO and H_2O in the warm environments of the disk, ice features and resolved images of scattered light.

New infrared and visible light instruments, like METIS at the future Extremely Large Telescope (ELT), will probe the disk surface through scattered light revealing signatures of dynamical interactions. SPHERE, at the Very Large Telescope (VLT) has already produced protoplanetary disks images in polarized light with high spatial resolution showing partially shadowed disks and spiral structures (e.g. Stolker et al. 2016a,b). Observations of polarized scattered light can be used to probe the complex small dust structure of the disk surface that respond to planet-disk interactions. In addition, direct-imaging of potential companions, with techniques such as polarized differential imaging, can help in distinguishing the different scenarios that shape the structures in the millimeter regime.

The interpretation of the observables presented in this thesis rely on state-of-the-art dust evolution models. At this stage, most models are not tailored to individual sources and their input variables are poorly constrained. A comprehensive treatment of gas and dust temperature coupled with chemistry and grain evolution is necessary to fully understand individual sources. Although individual sources are good laboratories to try detailed models, a statistically relevant large sample of different protoplanetary disks would average out individual differences. Large surveys would allow the disk community to focus on general trends in the structure of disks that can potentially lead to stronger conclusions and a more comprehensive understanding of the planet formation process.

Bibliography

Adams, F. C., Hollenbach, D., Laughlin, G., & Gorti, U. 2004, ApJ, 611, 360
Agúndez, M., Cernicharo, J., & Goicoechea, J. R. 2008, A&A, 483, 831
Aikawa, Y., Umebayashi, T., Nakano, T., & Miyama, S. M. 1999, ApJ, 519, 705
Aikawa, Y., van Zadelhoff, G. J., van Dishoeck, E. F., & Herbst, E. 2002, A&A, 386, 622
Aikawa, Y., Kamuro, D., Sakon, I., et al. 2012, A&A, 538, A57
Akimkin, V., Zhukovska, S., Wiebe, D., et al. 2013, ApJ, 766, 8
Albertsson, T., Semenov, D. A., Vasyunin, A. I., Henning, T., & Herbst, E. 2013, ApJS, 207, 27
ALMA Partnership, Brogan, C. L., Pérez, L. M., et al. 2015, ApJ, 808, L3
André, P., Ward-Thompson, D., & Barsony, M. 1993, ApJ, 406, 122
Andrews, S. M., Rosenfeld, K. A., Kraus, A. L., & Wilner, D. J. 2013, ApJ, 771, 129
Andrews, S. M., & Williams, J. P. 2005, ApJ, 631, 1134
Andrews, S. M., Wilner, D. J., Espaillat, C., et al. 2011, ApJ, 732, 42
Andrews, S. M., Wilner, D. J., Hughes, A. M., Qi, C., & Dullemond, C. P. 2009, ApJ, 700, 1502
Andrews, S. M., Wilner, D. J., Hughes, A. M., Qi, C., & Dullemond, C. P. 2010, ApJ, 723, 1241

Andrews, S. M., Wilner, D. J., Hughes, A. M., et al. 2012, ApJ, 744, 162
Andrews, S. M., Wilner, D. J., Zhu, Z., et al. 2016, ApJ, 820, L40
Ansdell, M., Williams, J. P., & Cieza, L. A. 2015, ApJ, 806, 221
Ansdell, M., Williams, J. P., Manara, C. F., et al. 2017, AJ, 153, 240
Ansdell, M., Williams, J. P., van der Marel, N., et al. 2016, ApJ, 828, 46
Arce, H. G., & Sargent, A. I. 2004, ApJ, 612, 342
Arce, H. G., & Sargent, A. I. 2006, ApJ, 646, 1070
Armitage, P. J. 2011, ARA&A, 49, 195
Atkinson, R., Baulch, D. L., Cox, R. A., et al. 2004, Atmospheric Chemistry & Physics, 4, 1461
Bacmann, A., Lefloch, B., Ceccarelli, C., et al. 2003, ApJ, 585, L55
Bai, X.-N. 2016, ApJ, 821, 80
Bally, J., O'Dell, C. R., & McCaughrean, M. J. 2000, AJ, 119, 2919
Barber, C. B., Dobkin, D. P., & Huhdanpaa, H. 1996, ACM Trans. Math. Softw., 22, 469
Barnes, R., Quinn, T. R., Lissauer, J. J., & Richardson, D. C. 2009, *Icarus*, 203, 626
Beckwith, S. V. W., Sargent, A. I., Chini, R. S., & Guesten, R. 1990, AJ, 99, 924
Bennett, C. J., Osamura, Y., Lebar, M. D., & Kaiser, R. I. 2005, ApJ, 634, 698
Benz, A. O., Bruderer, S., van Dishoeck, E. F., et al. 2010, A&A, 521, L35
Bergin, E., Calvet, N., D'Alessio, P., & Herczeg, G. J. 2003, ApJ, 591, L159
Bergin, E. A., & van Dishoeck, E. F. 2012, Philosophical Transactions of the Royal Society of London Series A, 370, 2778
Bergin, E. A., Cleeves, L. I., Gorti, U., et al. 2013, Nature, 493, 644
Bernstein, M. P., Sandford, S. A., Allamandola, L. J., Chang, S., & Scharberg, M. A. 1995, ApJ, 454, 327
Bethell, T., & Bergin, E. 2009, Science, 326, 1675
Birnstiel, T., & Andrews, S. M. 2014, ApJ, 780, 153
Birnstiel, T., Fang, M., & Johansen, A. 2016, Space Sci. Rev., 205, 41
Birnstiel, T., Klahr, H., & Ercolano, B. 2012, A&A, 539, A148
Birnstiel, T., Ormel, C. W., & Dullemond, C. P. 2011, A&A, 525, A11
Bjorkman, J. E., & Wood, K. 2001, ApJ, 554, 615
Bonnor, W. B. 1956, MNRAS, 116, 351
Boogert, A. C. A., Gerakines, P. A., & Whittet, D. C. B. 2015, ARA&A, 53, 541
Boogert, A. C. A., Pontoppidan, K. M., Knez, C., et al. 2008, ApJ, 678, 985
Bottinelli, S., Boogert, A. C. A., Bouwman, J., et al. 2010, ApJ, 718, 1100
Brauer, F., Henning, T., & Dullemond, C. P. 2008, A&A, 487, L1
Brinch, C. 2008, PhD thesis, Leiden University
Brinch, C., & Hogerheijde, M. R. 2010, A&A, 523, A25
Brown, J. M., Blake, G. A., Qi, C., et al. 2009, ApJ, 704, 496
Brown, P. D., & Millar, T. J. 1989, MNRAS, 240, 25P
Brownlee, D. 2014, Annual Review of Earth and Planetary Sciences, 42, 179
Burkert, A., & Bodenheimer, P. 2000, ApJ, 543, 822
Burrows, C. J., Stapelfeldt, K. R., Watson, A. M., et al. 1996, ApJ, 473, 437
Calvet, N., D'Alessio, P., Hartmann, L., et al. 2002, ApJ, 568, 1008
Calvet, N., Hartmann, L., Kenyon, S. J., & Whitney, B. A. 1994, ApJ, 434, 330
Cameron, A. G. W. 1978, Moon and Planets, 18, 5
Carney, M. T., Hogerheijde, M. R., Loomis, R. A., et al. 2017, A&A, 605, A21
Carney, M. T., Yıldız, U. A., Mottram, J. C., et al. 2016, A&A, 586, A44
Carr, J. S., & Najita, J. R. 2008, Science, 319, 1504
Carr, J. S., & Najita, J. R. 2011, ApJ, 733, 102
Caselli, P., & Ceccarelli, C. 2012, A&A Rev., 20, 56

Cassen, P., & Moosman, A. 1981, *Icarus*, 48, 353
Cernicharo, J., & Crovisier, J. 2005, Space Sci. Rev., 119, 29
Chapillon, E., Guilloteau, S., Dutrey, A., Piétu, V., & Guélin, M. 2012a, A&A, 537, A60
Chapillon, E., Dutrey, A., Guilloteau, S., et al. 2012b, ApJ, 756, 58
Cheung, A. C., Rank, D. M., Townes, C. H., Thornton, D. D., & Welch, W. J. 1968, Physical Review Letters, 21, 1701
Cheung, A. C., Rank, D. M., Townes, C. H., Thornton, D. D., & Welch, W. J. 1969, Nature, 221, 626
Chiang, E. I., & Goldreich, P. 1997, ApJ, 490, 368
Chiang, E. I., Joung, M. K., Creech-Eakman, M. J., et al. 2001, ApJ, 547, 1077
Cieza, L., Padgett, D. L., Stapelfeldt, K. R., et al. 2007, ApJ, 667, 308
Cieza, L. A., Casassus, S., Tobin, J., et al. 2016, Nature, 535, 258
Clarke, C. J. 2007, MNRAS, 376, 1350
Clarke, C. J., Gendrin, A., & Sotomayor, M. 2001, MNRAS, 328, 485
Cleeves, L. I., Bergin, E. A., Alexander, C. M. O. ., et al. 2014, Science, 345, 1590
Cohen, M., & Kuhi, L. V. 1979, ApJS, 41, 743
Combes, F., Boulanger, F., Encrenaz, P. J., et al. 1985, A&A, 147, L25
Cooke, R. J., Pettini, M., Nollett, K. M., & Jorgenson, R. 2016, ApJ, 830, 148
Cruz-Diaz, G. A., Muñoz Caro, G. M., & Jiménez-Escobar, A. 2012, in EAS Publications Series, Vol. 58, EAS Publications Series, ed. C. Stehlé, C. Joblin, & L. d'Hendecourt, 333–336
D'Alessio, P., Calvet, N., & Hartmann, L. 2001, ApJ, 553, 321
D'Alessio, P., Calvet, N., Hartmann, L., Franco-Hernández, R., & Servín, H. 2006, ApJ, 638, 314
D'Alessio, P., Cantö, J., Calvet, N., & Lizano, S. 1998, ApJ, 500, 411
Daranlot, J., Hincelin, U., Bergeat, A., et al. 2012, Proceedings of the National Academy of Science, 109, 10233
de Graauw, T., Helmich, F. P., Phillips, T. G., et al. 2010, A&A, 518, L6
de la Reza, R., Jilinski, E., & Ortega, V. G. 2006, AJ, 131, 2609
Debes, J. H., Jang-Condell, H., Weinberger, A. J., Roberge, A., & Schneider, G. 2013, ApJ, 771, 45
Dib, S., Hennebelle, P., Pineda, J. E., et al. 2010, ApJ, 723, 425
Dionatos, O. 2015, in European Physical Journal Web of Conferences, Vol. 102, European Physical Journal Web of Conferences, 00008
Draine, B. T. 2003, ARA&A, 41, 241
Draine, B. T. 2006, ApJ, 636, 1114
Dubrulle, B., Morfill, G., & Sterzik, M. 1995, *Icarus*, 114, 237
Dulieu, F., Amiaud, L., Congiu, E., et al. 2010, A&A, 512, A30
Dullemond, C. P., & Dominik, C. 2004a, A&A, 417, 159
Dullemond, C. P., & Dominik, C. 2004b, A&A, 421, 1075
Dullemond, C. P., & Dominik, C. 2005, A&A, 434, 971
Dullemond, C. P., & Dominik, C. 2008, A&A, 487, 205
Dullemond, C. P., Henning, T., Visser, R., et al. 2007, A&A, 473, 457
Dunham, M. M., Arce, H. G., Mardones, D., et al. 2014, ApJ, 783, 29
Dutrey, A., Guilloteau, S., & Guelin, M. 1997, A&A, 317, L55
Dutrey, A., Wakelam, V., Boehler, Y., et al. 2011, A&A, 535, A104
Ebert, R. 1955, in Liege International Astrophysical Colloquia, Vol. 6, Liege International Astrophysical Colloquia, 666–672
Elitzur, M., & Watson, W. D. 1978, ApJ, 222, L141
Evans, N. J., Dunham, M. M., Jorgensen, J. K., et al. 2009, VizieR Online Data Catalog, 218

Facchini, S., Birnstiel, T., Bruderer, S., & van Dishoeck, E. F. 2017, A&A, 605, A16
Favre, C., Bergin, E. A., Cleeves, L. I., et al. 2015, ApJ, 802, L23
Fayolle, E. C., Öberg, K. I., Cuppen, H. M., Visser, R., & Linnartz, H. 2011, A&A, 529, A74
Fedele, D., Bruderer, S., van Dishoeck, E. F., et al. 2012, A&A, 544, L9
Fedele, D., van den Ancker, M. E., Henning, T., Jayawardhana, R., & Oliveira, J. M. 2010, A&A, 510, A72
Fedele, D., Bruderer, S., van Dishoeck, E. F., et al. 2013, A&A, 559, A77
Fedoseev, G., Chuang, K.-J., Ioppolo, S., et al. 2017, ApJ, 842, 52
Fedoseev, G., Ioppolo, S., Zhao, D., Lamberts, T., & Linnartz, H. 2015, MNRAS, 446, 439
Flower, D. R., Pineau Des Forêts, G., & Walmsley, C. M. 2006, A&A, 449, 621
Fogel, J. K. J., Bethell, T. J., Bergin, E. A., Calvet, N., & Semenov, D. 2011, ApJ, 726, 29
Furuya, K., & Aikawa, Y. 2014, ApJ, 790, 97
Garaud, P., Meru, F., Galvagni, M., & Olczak, C. 2013, ApJ, 764, 146
Garrod, R. T., Wakelam, V., & Herbst, E. 2007, A&A, 467, 1103
Genzel, R. 1992, in Saas-Fee Advanced Course 21: The Galactic Interstellar Medium, ed. W. B. Burton, B. G. Elmegreen, & R. Genzel, 275–391
Gerner, T., Shirley, Y. L., Beuther, H., et al. 2015, A&A, 579, A80
Getman, K. V., Feigelson, E. D., Luhman, K. L., et al. 2009, ApJ, 699, 1454
Gibb, E. L., Whittet, D. C. B., Boogert, A. C. A., & Tielens, A. G. G. M. 2004, ApJS, 151, 35
Gillett, F. C., & Forrest, W. J. 1973, ApJ, 179, 483
Goodman, A. A., Benson, P. J., Fuller, G. A., & Myers, P. C. 1993, ApJ, 406, 528
Gorti, U., Dullemond, C. P., & Hollenbach, D. 2009, ApJ, 705, 1237
Gorti, U., & Hollenbach, D. 2004, ApJ, 613, 424
Greaves, J. S., & Rice, W. K. M. 2010, MNRAS, 407, 1981
Greenberg, R., Hartmann, W. K., Chapman, C. R., & Wacker, J. F. 1978, *Icarus*, 35, 1
Griffin, M. J., Abergel, A., Abreu, A., et al. 2010, A&A, 518, L3
Güdel, M., & Nazé, Y. 2009, A&A Rev., 17, 309
Haghighipour, N. 2013, Annual Review of Earth and Planetary Sciences, 41, 469
Harada, N., Herbst, E., & Wakelam, V. 2010, ApJ, 721, 1570
Harju, J., Daniel, F., Sipilä, O., et al. 2017, A&A, 600, A61
Harker, D. E., & Desch, S. J. 2002, ApJ, 565, L109
Harries, T. J. 2000, MNRAS, 315, 722
Harries, T. J., Monnier, J. D., Symington, N. H., & Kurosawa, R. 2004, MNRAS, 350, 565
Harsono, D. 2014, PhD thesis, Leiden University, doi:10.5281/zenodo.29224
Hartmann, L., Calvet, N., Gullbring, E., & D'Alessio, P. 1998, ApJ, 495, 385
Hasegawa, T. I., & Herbst, E. 1993, MNRAS, 261, 83
Hayashi, C. 1981, Progress of Theoretical Physics Supplement, 70, 35
Heays, A. N., Bosman, A. D., & van Dishoeck, E. F. 2017, A&A, 602, A105
Henning, T., & Semenov, D. 2013, Chemical Reviews, 113, 9016
Henning, T., Semenov, D., Guilloteau, S., et al. 2010, ApJ, 714, 1511
Herbig, G. H. 1977, ApJ, 214, 747
Herbst, E., & Klemperer, W. 1973, ApJ, 185, 505
Herbst, E., & van Dishoeck, E. F. 2009, ARA&A, 47, 427
Hildebrand, R. H. 1983, QJRAS, 24, 267
Hirose, S., & Turner, N. J. 2011, ApJ, 732, L30
Hoff, W., Henning, T., & Pfau, W. 1998, A&A, 336, 242
Hogerheijde, M., & van der Tak, F. 2000, RATRAN: Radiative Transfer and Molecular Excitation in One and Two Dimensions, Astrophysics Source Code Library, ascl:0008.002
Hogerheijde, M. R., Bergin, E. A., Brinch, C., et al. 2011, Science, 334, 338

Hueso, R., & Guillot, T. 2005, A&A, 442, 703
Hughes, A. M., Wilner, D. J., Andrews, S. M., Qi, C., & Hogerheijde, M. R. 2011, ApJ, 727, 85
Hughes, A. M., Wilner, D. J., Qi, C., & Hogerheijde, M. R. 2008, ApJ, 678, 1119
Ida, S., & Makino, J. 1993, *Icarus*, 106, 210
Ilgner, M., Henning, T., Markwick, A. J., & Millar, T. J. 2004, A&A, 415, 643
Ioppolo, S., Cuppen, H. M., Romanzin, C., van Dishoeck, E. F., & Linnartz, H. 2008, ApJ, 686, 1474
Irvine, W. M., Goldsmith, P. F., & Hjalmarson, A. 1987, in Astrophysics and Space Science Library, Vol. 134, Interstellar Processes, ed. D. J. Hollenbach & H. A. Thronson, Jr., 561–609
Irvine, W. M., Schloerb, F. P., Crovisier, J., Fegley, Jr., B., & Mumma, M. J. 2000, Protostars and Planets IV, 1159
Isella, A., Carpenter, J. M., & Sargent, A. I. 2009, ApJ, 701, 260
Isella, A., Testi, L., Natta, A., et al. 2007, A&A, 469, 213
Isella, A., Guidi, G., Testi, L., et al. 2016, Physical Review Letters, 117, 251101
Jeans, J. H. 1902, Philosophical Transactions of the Royal Society of London Series A, 199, 1
Johansen, A., Oishi, J. S., Mac Low, M.-M., et al. 2007, Nature, 448, 1022
Jonkheid, B., Kamp, I., Augereau, J.-C., & van Dishoeck, E. F. 2006, A&A, 453, 163
Kastner, J. H., Zuckerman, B., Weintraub, D. A., & Forveille, T. 1997, Science, 277, 67
Kataoka, A., Tsukagoshi, T., Momose, M., et al. 2016, ApJ, 831, L12
Kennedy, G. M., & Kenyon, S. J. 2008, ApJ, 673, 502
Kenyon, S. J., & Hartmann, L. 1987, ApJ, 323, 714
Kenyon, S. J., & Hartmann, L. W. 1990, ApJ, 349, 197
Kessler-Silacci, J. E., Dullemond, C. P., Augereau, J.-C., et al. 2007, ApJ, 659, 680
Knacke, R. F., McCorkle, S., Puetter, R. C., Erickson, E. F., & Kraetschmer, W. 1982, ApJ, 260, 141
Königl, A., & Salmeron, R. 2011, The Effects of Large-Scale Magnetic Fields on Disk Formation and Evolution, ed. P. J. V. Garcia, 283–352
Lada, C. J. 1987, in IAU Symposium, Vol. 115, Star Forming Regions, ed. M. Peimbert & J. Jugaku, 1–17
Lahuis, F., van Dishoeck, E. F., Boogert, A. C. A., et al. 2006, ApJ, 636, L145
Lambrechts, M., & Johansen, A. 2014, A&A, 572, A107
Le Gal, R., Hily-Blant, P., Faure, A., et al. 2014, A&A, 562, A83
Lee, N., Williams, J. P., & Cieza, L. A. 2011, ApJ, 736, 135
Leger, A., Jura, M., & Omont, A. 1985, A&A, 144, 147
Lissauer, J. J. 1993, ARA&A, 31, 129
Lissauer, J. J., Marcy, G. W., Rowe, J. F., et al. 2012, ApJ, 750, 112
Lucy, L. B. 1999, A&A, 345, 211
Lynden-Bell, D., & Pringle, J. E. 1974, MNRAS, 168, 603
Lyra, W., Johansen, A., Zsom, A., Klahr, H., & Piskunov, N. 2009, A&A, 497, 869
Malfait, K., Waelkens, C., Bouwman, J., de Koter, A., & Waters, L. B. F. M. 1999, A&A, 345, 181
Mandell, A. M., Bast, J., van Dishoeck, E. F., et al. 2012, ApJ, 747, 92
Mann, R. K., & Williams, J. P. 2009, ApJ, 699, L55
Markwick, A. J., Ilgner, M., Millar, T. J., & Henning, T. 2002, A&A, 385, 632
Matthews, G. S., Klaassen, P. D., Juhász, A., et al. 2013, A&A, 557, A132
Mathis, J. S., Rumpl, W., & Nordsieck, K. H. 1977, ApJ, 217, 425
Matsuyama, I., Johnstone, D., & Hollenbach, D. 2009, ApJ, 700, 10

Mayor, M., & Queloz, D. 1995, Nature, 378, 355
McCaughrean, M. J., & O'dell, C. R. 1996, AJ, 111, 1977
McClure, M. K., Furlan, E., Manoj, P., et al. 2010, ApJS, 188, 75
McClure, M. K., Manoj, P., Calvet, N., et al. 2012, ApJ, 759, L10
Meeus, G., Montesinos, B., Mendigutía, I., et al. 2012, A&A, 544, A78
Meeus, G., Salyk, C., Bruderer, S., et al. 2013, A&A, 559, A84
Melnick, G. J. 2009, in Astronomical Society of the Pacific Conference Series, Vol. 417, Submillimeter Astrophysics and Technology: a Symposium Honoring Thomas G. Phillips, ed. D. C. Lis, J. E. Vaillancourt, P. F. Goldsmith, T. A. Bell, N. Z. Scoville, & J. Zmuidzinas, 59
Merrill, K. M., Russell, R. W., & Soifer, B. T. 1976, ApJ, 207, 763
Millar, T. J., Bennett, A., & Herbst, E. 1989, ApJ, 340, 906
Miotello, A., van Dishoeck, E. F., Kama, M., & Bruderer, S. 2016, A&A, 594, A85
Miyauchi, N., Hidaka, H., Chigai, T., et al. 2008, Chemical Physics Letters, 456, 27
Moore, M. H., & Hudson, R. L. 1998, *Icarus*, 135, 518
Morbidelli, A., Chambers, J., Lunine, J. I., et al. 2000, Meteoritics and Planetary Science, 35, 1309
Mordasini, C., Alibert, Y., Benz, W., Klahr, H., & Henning, T. 2012, A&A, 541, A97
Morris, M., Zuckerman, B., Palmer, P., & Turner, B. E. 1973, ApJ, 186, 501
Mumma, M. J., & Charnley, S. B. 2011, ARA&A, 49, 471
Najita, J., Bergin, E. A., & Ullom, J. N. 2001, ApJ, 561, 880
Najita, J. R., Ádámkovics, M., & Glassgold, A. E. 2011, ApJ, 743, 147
Nakagawa, Y., Sekiya, M., & Hayashi, C. 1986, *Icarus*, 67, 375
Natta, A. 1993, ApJ, 412, 761
Natta, A., Grinin, V., & Mannings, V. 2000, Protostars and Planets IV, 559
Natta, A., Testi, L., Neri, R., Shepherd, D. S., & Wilner, D. J. 2004, A&A, 416, 179
Öberg, K. I. 2009, PhD thesis, Leiden University
Öberg, K. I., Boogert, A. C. A., Pontoppidan, K. M., et al. 2011a, ApJ, 740, 109
Öberg, K. I., Fuchs, G. W., Awad, Z., et al. 2007, ApJ, 662, L23
Öberg, K. I., Furuya, K., Loomis, R., et al. 2015, ApJ, 810, 112
Öberg, K. I., Linnartz, H., Visser, R., & van Dishoeck, E. F. 2009a, ApJ, 693, 1209
Öberg, K. I., Qi, C., Wilner, D. J., & Andrews, S. M. 2011b, ApJ, 743, 152
Öberg, K. I., Qi, C., Wilner, D. J., & Hogerheijde, M. R. 2012, ApJ, 749, 162
Öberg, K. I., van Dishoeck, E. F., & Linnartz, H. 2009b, A&A, 496, 281
Öberg, K. I., Qi, C., Fogel, J. K. J., et al. 2010, ApJ, 720, 480
Öberg, K. I., Qi, C., Fogel, J. K. J., et al. 2011c, ApJ, 734, 98
Oliveira, I., Olofsson, J., Pontoppidan, K. M., et al. 2011, ApJ, 734, 51
Olofsson, J., Augereau, J.-C., van Dishoeck, E. F., et al. 2010, A&A, 520, A39
Olofsson, J., Augereau, J.-C., van Dishoeck, E. F., et al. 2009, A&A, 507, 327
Ormel, C. W., & Klahr, H. H. 2010, A&A, 520, A43
Ossenkopf, V., & Henning, T. 1994, A&A, 291, 943
Owen, J. E., Ercolano, B., Clarke, C. J., & Alexander, R. D. 2010, MNRAS, 401, 1415
Padgett, D. L., Brandner, W., Stapelfeldt, K. R., et al. 1999, AJ, 117, 1490
Pagani, L., Vastel, C., Hugo, E., et al. 2009, A&A, 494, 623
Panić, O., Hogerheijde, M. R., Wilner, D., & Qi, C. 2009, A&A, 501, 269
Pascucci, I., Apai, D., Luhman, K., et al. 2009, ApJ, 696, 143
Pavlyuchenkov, Y., & Dullemond, C. P. 2007, A&A, 471, 833
Pérez, L. M., Carpenter, J. M., Andrews, S. M., et al. 2016, Science, 353, 1519
Perryman, M. A. C., Lindegren, L., Kovalevsky, J., et al. 1997, A&A, 323, L49

Persson, C. M., Black, J. H., Cernicharo, J., et al. 2010, A&A, 521, L45
Pfalzner, S., Umbreit, S., & Henning, T. 2005a, ApJ, 629, 526
Pfalzner, S., Vogel, P., Scharwächter, J., & Olczak, C. 2005b, A&A, 437, 967
Piétu, V., Dutrey, A., Guilloteau, S., Chapillon, E., & Pety, J. 2006, A&A, 460, L43
Piétu, V., Guilloteau, S., & Dutrey, A. 2005, A&A, 443, 945
Pinilla, P., van der Marel, N., Pérez, L. M., et al. 2015, A&A, 584, A16
Pinte, C., Harries, T. J., Min, M., et al. 2009, A&A, 498, 967
Pinto, R. F., Brun, A. S., Jouve, L., & Grappin, R. 2011, ApJ, 737, 72
Poglitsch, A., Waelkens, C., Geis, N., et al. 2010, A&A, 518, L2
Pollack, J. B., Hollenbach, D., Beckwith, S., et al. 1994, ApJ, 421, 615
Pollack, J. B., Hubickyj, O., Bodenheimer, P., et al. 1996, *Icarus*, 124, 62
Pontoppidan, K. M., Dullemond, C. P., van Dishoeck, E. F., et al. 2005, ApJ, 622, 463
Pontoppidan, K. M., Salyk, C., Blake, G. A., & Käufl, H. U. 2010, ApJ, 722, L173
Prasad, S. S., & Tarafdar, S. P. 1983, ApJ, 267, 603
Preibisch, T., Kim, Y.-C., Favata, F., et al. 2005, ApJS, 160, 401
Prodanović, T., Steigman, G., & Fields, B. D. 2010, MNRAS, 406, 1108
Qi, C., D'Alessio, P., Öberg, K. I., et al. 2011, ApJ, 740, 84
Qi, C., Öberg, K. I., Andrews, S. M., et al. 2015, ApJ, 813, 128
Qi, C., Ho, P. T. P., Wilner, D. J., et al. 2004, ApJ, 616, L11
Qi, C., Öberg, K. I., Wilner, D. J., et al. 2013, Science, 341, 630
Riviere-Marichalar, P., Merín, B., Kamp, I., Eiroa, C., & Montesinos, B. 2016, A&A, 594, A59
Riviere-Marichalar, P., Ménard, F., Thi, W. F., et al. 2012, A&A, 538, L3
Roberts, H., Fuller, G. A., Millar, T. J., Hatchell, J., & Buckle, J. V. 2002, Planet. Space Sci., 50, 1173
Roueff, E., Loison, J. C., & Hickson, K. M. 2015, A&A, 576, A99
Safronov, V. S. 1972, Evolution of the protoplanetary cloud and formation of the earth and planets. (Israel Program for Scientific Translations, Keter Publishing House, 212 p.)
Salter, D. M. 2010, PhD thesis, Leiden University
Salyk, C., Pontoppidan, K. M., Blake, G. A., et al. 2008, ApJ, 676, L49
Salyk, C., Pontoppidan, K. M., Blake, G. A., Najita, J. R., & Carr, J. S. 2011, ApJ, 731, 130
Schöier, F. L., van der Tak, F. F. S., van Dishoeck, E. F., & Black, J. H. 2005, A&A, 432, 369
Schreyer, K., Guilloteau, S., Semenov, D., et al. 2008, A&A, 491, 821
Semenov, D., Pavlyuchenkov, Y., Schreyer, K., et al. 2005, ApJ, 621, 853
Semenov, D., & Wiebe, D. 2011, ApJS, 196, 25
Shakura, N. I., Sunyaev, R. A., & Zilitinkevich, S. S. 1978, A&A, 62, 179
Sipilä, O., Harju, J., Caselli, P., & Schlemmer, S. 2015, A&A, 581, A122
Smith, N., Bally, J., Licht, D., & Walawender, J. 2005, AJ, 129, 382
Smith, R. G., Sellgren, K., & Tokunaga, A. T. 1989, ApJ, 344, 413
Stapelfeldt, K. R., Burrows, C. J., Krist, J. E., et al. 1998, ApJ, 508, 736
Stolker, T., Dominik, C., Min, M., et al. 2016a, A&A, 596, A70
Stolker, T., Dominik, C., Avenhaus, H., et al. 2016b, A&A, 595, A113
Sturm, B., Bouwman, J., Henning, T., et al. 2010, A&A, 518, L129
Terada, H., & Tokunaga, A. T. 2017, ApJ, 834, 115
Terada, H., Tokunaga, A. T., Kobayashi, N., et al. 2007, ApJ, 667, 303
Terebey, S., Shu, F. H., & Cassen, P. 1984, ApJ, 286, 529
Thi, W. F., Pontoppidan, K. M., van Dishoeck, E. F., Dartois, E., & d'Hendecourt, L. 2002, A&A, 394, L27
Thi, W.-F., van Zadelhoff, G.-J., & van Dishoeck, E. F. 2004, A&A, 425, 955
Thies, I., Kroupa, P., Goodwin, S. P., Stamatellos, D., & Whitworth, A. P. 2010, ApJ, 717, 577

Tielens, A. G. G. M. 1983, A&A, 119, 177
Tielens, A. G. G. M. 2008, ARA&A, 46, 289
Turner, B. E. 2001, ApJS, 136, 579
Turner, N. J., Fromang, S., Gammie, C., et al. 2014, Protostars and Planets VI, 411
Ulrich, R. K. 1976, ApJ, 210, 377
Vacca, W. D., & Sandell, G. 2011, ApJ, 732, 8
van Boekel, R., Min, M., Waters, L. B. F. M., et al. 2005, A&A, 437, 189
van de Hulst, H. C. 1946, Recherches Astronomiques de l'Observatoire d'Utrecht, 11, 2.i
van der Marel, N., van Dishoeck, E. F., Bruderer, S., et al. 2013, Science, 340, 1199
van Dishoeck, E. F. 2004, ARA&A, 42, 119
van Dishoeck, E. F. 2006, Proceedings of the National Academy of Science, 103, 12249
van Dishoeck, E. F., Bergin, E. A., Lis, D. C., & Lunine, J. I. 2014, Protostars and Planets VI, 835
van Dishoeck, E. F., & Black, J. H. 1988, ApJ, 334, 771
van Dishoeck, E. F., Jonkheid, B., & van Hemert, M. C. 2006, Faraday Discussions, 133, 231
van Dishoeck, E. F., Kristensen, L. E., Benz, A. O., et al. 2011, PASP, 123, 138
van Leeuwen, F. 2007, A&A, 474, 653
van Zadelhoff, G.-J., Aikawa, Y., Hogerheijde, M. R., & van Dishoeck, E. F. 2003, A&A, 397, 789
van Zadelhoff, G.-J., van Dishoeck, E. F., Thi, W.-F., & Blake, G. A. 2001, A&A, 377, 566
Vastel, C., Caselli, P., Ceccarelli, C., et al. 2006, ApJ, 645, 1198
Vasyunin, A. I., Wiebe, D. S., Birnstiel, T., et al. 2011, ApJ, 727, 76
Velusamy, T., & Langer, W. D. 1998, Nature, 392, 685
Vicente, S. M., & Alves, J. 2005, A&A, 441, 195
Visser, R. 2009, PhD thesis, Ph. D. thesis, Leiden University
Wakelam, V., Herbst, E., Loison, J.-C., et al. 2012, ApJS, 199, 21
Walsh, C., Millar, T. J., & Nomura, H. 2010, ApJ, 722, 1607
Walsh, C., Millar, T. J., Nomura, H., et al. 2014, A&A, 563, A33
Walsh, C., Nomura, H., Millar, T. J., & Aikawa, Y. 2012, ApJ, 747, 114
Walsh, C., Nomura, H., & van Dishoeck, E. 2015, A&A, 582, A88
Walsh, C., Loomis, R. A., Öberg, K. I., et al. 2016, ApJ, 823, L10
Watson, W. D. 1974, ApJ, 188, 35
Watson, W. D. 1976, Reviews of Modern Physics, 48, 513
Webb, R. A., Zuckerman, B., Platais, I., et al. 1999, ApJ, 512, L63
Weidenschilling, S. J. 1977, MNRAS, 180, 57
Weidenschilling, S. J. 1984, *Icarus*, 60, 553
Whittet, D. C. B., Shenoy, S. S., Bergin, E. A., et al. 2007, ApJ, 655, 332
Willacy, K. 2007, ApJ, 660, 441
Willacy, K., & Millar, T. J. 1998, MNRAS, 298, 562
Williams, J. P., & Best, W. M. J. 2014, ApJ, 788, 59
Williams, J. P., & Cieza, L. A. 2011, ARA&A, 49, 67
Williams, J. P., Cieza, L. A., Andrews, S. M., et al. 2013, MNRAS, 435, 1671
Windmark, F., Birnstiel, T., Güttler, C., et al. 2012, A&A, 540, A73
Woodall, J., Agúndez, M., Markwick-Kemper, A. J., & Millar, T. J. 2007, A&A, 466, 1197
Woods, P. M., & Willacy, K. 2007, ApJ, 655, L49
Yorke, H. W., Bodenheimer, P., & Laughlin, G. 1993, ApJ, 411, 274
Youdin, A. N., & Lithwick, Y. 2007, *Icarus*, 192, 588
Zhang, K., Bergin, E. A., Blake, G. A., et al. 2016, ApJ, 818, L16
Zhang, Y., & Jin, L. 2015, ApJ, 802, 58

Zinnecker, H., & Yorke, H. W. 2007, ARA&A, 45, 481